Monthly Notices
of the
ROYAL ASTRONOMICAL SOCIETY

MNRAS **461,** 1981–2002 (2016)
Advance Access publication 2016 May 30

doi:10.1093/mnras/stw1265

Connecting the dots – III. Nightside cooling and surface friction affect climates of tidally locked terrestrial planets

L. Carone,[1]★ R. Keppens[1] and L. Decin[2]

[1]*Centre for Mathematical Plasma Astrophysics, Department of Mathematics, KU Leuven, Celestijnenlaan 200B, 3001 Leuven, Belgium*
[2]*Instituut voor Sterrenkunde, KU Leuven, Celestijnenlaan 200D, 3001 Leuven, Belgium*

Accepted 2016 May 25. Received 2016 May 25; in original form 2015 September 18

ABSTRACT

We investigate how nightside cooling and surface friction affect surface temperatures and large-scale circulation for tidally locked Earth-like planets. For each scenario, we vary the orbital period between $P_{\rm rot} = 1$ and 100 d and capture changes in climate states. We find drastic changes in climate states for different surface friction scenarios. For very efficient surface friction ($t_{\rm s,fric} = 0.1$ d), the simulations for short rotation periods ($P_{\rm rot} \leq 10$ d) show predominantly standing extratropical Rossby waves. These waves lead to climate states with two high-latitude westerly jets and unperturbed meridional direct circulation. In most other scenarios, simulations with short rotation periods exhibit instead dominance by standing tropical Rossby waves. Such climate states have a single equatorial westerly jet, which disrupts direct circulation. Experiments with weak surface friction ($t_{\rm s,fric} = 10$–100 d) show decoupling between surface temperatures and circulation, which leads to strong cooling of the nightside. The experiment with $t_{\rm s,fric} = 100$ d assumes climate states with easterly flow (retrograde rotation) for medium and slow planetary rotations $P_{\rm rot} = 12$–100 d. We show that an increase of nightside cooling efficiency by one order of magnitude compared to the nominal model leads to a cooling of the nightside surface temperatures by 80–100 K. The dayside surface temperatures only drop by 25 K at the same time. The increase in thermal forcing suppresses the formation of extratropical Rossby waves on small planets ($R_{\rm P} = 1 R_{\rm Earth}$) in the short rotation period regime ($P_{\rm rot} \leq 10$ d).

Key words: methods: numerical – planets and satellites: atmospheres – planets and satellites: terrestrial planets.

1 INTRODUCTION

The climate states of tidally locked terrestrial planets do not fail to surprise. Joshi, Haberle & Reynolds (1997) found that a sufficiently dense atmosphere (i.e. with surface pressure level $p_{\rm s} \geq 100$ mbar) can maintain generally habitable surface temperatures – even with one planet side permanently facing their host star. Recently, Yang et al. (2014) found that cloud coverage over the substellar point leads to a net cooling of the atmosphere, in contrast to fast rotating non-tidally locked planets. This stabilizing cloud feedback pushes the inner edge of the habitable zone closer towards the star. Even more recently, Carone, Keppens & Decin (2015, hereafter Paper II) found that fast rotating tidally locked planets ($P_{\rm orb} = P_{\rm rot} \leq 12$ d for large terrestrial planets) can assume up to three different climate states, depending on the dominance of either the tropical or extratropical standing Rossby waves, or a mixture of both.

Merlis & Schneider (2010) report for $P_{\rm rot} = 1$ d two high-latitude westerly jets, which we linked in Paper II to the dominance of a standing extratropical Rossby wave. Edson et al. (2011) show for their dry model and the same rotation period a mixed climate state with two high-latitude westerly jets and tropical jets, apparently induced by the simultaneous presence of standing tropical and extratropical Rossby waves. In Paper II, for $P_{\rm rot} = 1$ d, we reported one single equatorial wind jet with very fast wind speeds (about 300 m s^{-1}), which we linked to the dominance of a standing tropical Rossby wave.

These three models differ from each other in that Merlis & Schneider (2010) study the climate of an aquaplanet with moderate dayside to nightside temperature gradient. The authors report maximum surface temperatures of $T_{\rm DS,s} = 300$ K at the dayside and minimum temperatures of $T_{\rm NS,s} = 250$ K at the nightside. Edson et al. (2011) assume for one of their climate models a completely dry surface, which leads to a stronger horizontal surface temperature gradient. They have maximum temperatures of $T_{\rm DS,s} = 350$ K at the dayside and minimum temperatures of $T_{\rm NS,s} = 150$–170 K

★ E-mail: ludmila.carone@wis.kuleuven.be

at the nightside. Our nominal model falls in between, in that it has a relatively warm dayside with maximum dayside surface temperatures of up to $T_{\rm DS,s} = 370$ K for $P_{\rm rot} = 1$ d and relatively high minimum nightside temperatures of $T_{\rm NS,s} = 270$ K for an Earth-size planet. Our model, however, has the advantage that we can perform large parametric surveys at low computational cost. Because of the model's transparent and versatile parametrization, we can identify possible sources of deviation and have full control over optical depth, effective radiative time-scales on the dayside and nightside, surface friction time-scales and the extent of the surface boundary layer.

Indeed, we already identified in Carone, Keppens & Decin (2014, hereafter Paper I) low nightside cooling efficiency as the likely origin for the comparatively warm nightside and thus as one source of deviations between our nominal model and that of Edson et al. (2011) and Joshi (2003).

Another notorious source for deviations between climate models on terrestrial planets are surface boundary prescriptions that vary even for terrestrial Solar system planets by orders of magnitude (Paper I). In this paper, we show that different nightside cooling efficiencies and, in particular, surface boundary treatments affect climate patterns in the rotation period regime $P_{\rm rot} = 1$–100 d.

Because of the computational efficiency of our model, we can perform many simulations for tidally locked planets between $P_{\rm rot} = 1$ and 100 d. We can thus monitor closely changes in climate state transitions with planet rotation. This resolution in rotation period is so far unrivalled. By checking the tropical ($\lambda_{\rm R}$) and extratropical ($L_{\rm R}$) Rossby radius of deformation and by performing a perturbation analysis on the horizontal velocity $\boldsymbol{v}$ and geopotential height z (see Paper II), we can furthermore coherently link climate state phases to tropical and extratropical Rossby waves.

First, in Section 2, we briefly describe the model and the numerical adjustments for very short orbital periods, and we introduce the relevant parameter space for tidally locked habitable planets. Then, in Section 3, we systematically investigate how an increase of the nightside cooling efficiency changes surface temperatures. We also account for differences in optical depths and planet sizes. Furthermore, we investigate how more efficient nightside cooling affects climate state transitions for specific Rossby radii of deformation over planet size, that is, for $\lambda_{\rm R}/R_{\rm P} = 1$ and 0.5 and $L_{\rm R}/R_{\rm P} = 1$ and 0.5. We also compare our results to other tidally locked Earth climate models, as in Joshi et al. (1997), Edson et al. (2011) and Joshi (2003).

For the investigation of different frictional surface boundary treatments on climate states, in Section 4, we use our nominal model on a Super-Earth planet[1] ($R_{\rm P} = 1.45\,R_{\rm Earth}$). We study surface friction time-scales between $t_{\rm fric} = 0.1$ and 100 d and change the upper extent of the planet boundary layer to values between 70 and 90 per cent of surface pressure level $p_{\rm s}$. These ranges of values were identified in Paper I from climate models of Solar system terrestrial planets. For every scenario, we again monitor climate state transitions in Rossby waves for $\lambda_{\rm R}/R_{\rm P} = 1$ and 0.5 and $L_{\rm R}/R_{\rm P} = 1$ and 0.5. In Section 5, we provide a summary of our results, and in Section 6 we give a conclusion and outlook.

This is the first study to coherently investigate different assumptions in nightside cooling efficiency and surface friction time-scales and how they affect surface temperatures on tidally locked habitable planets over the whole relevant rotation period range. Thus, this study will provide a better understanding of surface temperatures arising from different climate models for tidally locked terrestrial planets.

2 OUR MODEL

We introduced in Paper I our nominal three-dimensional (3D) climate model with simplified forcing that is suitable for a tidally locked terrestrial planet. The model uses Newtonian cooling for the thermal forcing of the dynamical core of the Massachusetts Institute of Technology global circulation model[2] (MITgcm; Adcroft et al. 2004). MITgcm uses the finite-volume method to solve the primitive hydrostatical equations that can be written as the horizontal momentum, vertical stratification, continuity of mass, equation of state for an ideal gas and thermal forcing equation (see equations 1–6 in Paper II).

A first-order estimate is used for the radiative time-scale $t_{\rm rad}$ in the Newtonian thermal forcing that agrees within one order of magnitude to values derived with full radiative transfer for terrestrial Solar system planets (Paper I). The details of thermal forcing are further discussed in Section 3. The details of surface boundary treatments, where we use a simple Rayleigh friction scheme for the near-surface part of the atmosphere, are further discussed in Section 4.

2.1 Numerical set-up

We use 20 vertical levels with equally spaced 50-mbar levels with surface pressure $p_{\rm s} = 1000$ mbar. The C32 cubed-sphere grid is used (Marshall et al. 2004). The sphere is subdivided into six tiles, each with 32×32 elements, and thus there are $32 \times 32 \times 20$ volume elements per tile. This grid corresponds to a global resolution in longitude–latitude of 128×64 or approximately $2.^{\circ}8 \times 2.^{\circ}8$.

As outlined in Paper I, we initialize the atmosphere with constant temperature $T = 264$ K and run for $t_{\rm init} = 400$ d. Data generated before $t_{\rm init}$ are discarded; the simulation is run subsequently for $t_{\rm run} = 1000$ d and averaged over this time period. The nominal time-step is $\Delta t = 450$ s; however, the smallest investigated planet size, $R_{\rm P} = 1\,R_{\rm Earth}$, requires a reduction to $\Delta t = 300$ s (see also Paper II). The horizontal momentum forcing $\boldsymbol{F}_{v} = \boldsymbol{F}_{\rm fric} + \boldsymbol{F}_{\rm sponge}$ consists of a surface friction (to be discussed in Section 4) and a sponge layer term, which we prescribe as

$$\boldsymbol{F}_{\rm sponge} = -k_{\rm R}\boldsymbol{v}, \tag{1}$$

where $k_{\rm R}$ determines the efficiency of horizontal wind braking in the sponge layer.

The sponge layer stabilizes the upper atmosphere boundary layer against non-physical wave reflection. It can also be justified physically as a first-order representation of gravity wave breaking at low atmosphere pressure. The sponge layer is located at pressures less than $p = 100$ mbar, where $k_{\rm R}$ increases from zero to $k_{\rm max}$ with decreasing pressure using the prescription of Polvani & Kushner (2002) (see Paper I). In the nominal set-up, $k_{\rm max}$ was set to $1/80\ {\rm d}^{-1}$. Simulations with fast rotations ($P_{\rm rot} \leq 4$ d) show very fast equatorial superrotation at the top of the atmosphere with wind speeds of up to $300\ {\rm m\,s}^{-1}$. The very fast winds require a larger efficiency of the upper atmosphere sponge layer. See Table 1 for relevant parameters.

We adopted the dry convection scheme of Molteni (2002) for our model that diffuses dry static energy $s = c_{\rm P}T + \Phi$ vertically

[1] We choose $R_{\rm P} = 1.45\,R_{\rm Earth}$ instead of $R_{\rm P} = 1.5\,R_{\rm Earth}$ to be comparable to Paper I.

[2] http://mitgcm.org

Table 1. Sponge layer friction time-scales used this study.

k_{max} (d^{-1})	P_{rot} (d)
1/80	5–100
1/40	3–4
1/20 for optical depth $\tau_s = 0.62$ 1/10 for optical depth $\tau_s = 0.94$	≤2

with vertical diffusion time-scale t_{vds}, if static stability is locally violated. Here, c_P is specific heat at constant pressure and $\Phi = gz$ is the geopotential, where g is surface gravity and z is vertical height. In the nominal model and most simulations discussed in this study, the vertical diffusion time-scale $t_{vds} = 1$ d is assumed as in Papers I and II.

2.2 Investigated parameter space: tidally locked habitable terrestrial planets around M dwarfs

We focus on atmosphere dynamics of tidally locked habitable planets around M dwarfs and assume the same set-up as in Paper I: a nitrogen-dominated greenhouse atmosphere with surface pressure $p_s = 1000$ mbar. We further assume that each planet receives the same amount of stellar irradiation as the Earth. See Table 2 for the relevant planetary parameters.

Correia, Levrard & Laskar (2008) and, more recently, Leconte et al. (2015) questioned the assumption that terrestrial planets in the habitable zone of an M dwarf are tidally locked. Thus, the climate of a terrestrial planet in the habitable zone must be interpreted in the context of two extremes in spin-orbit alignment: fast rotating asynchronous rotations, such as the Earth, and tidal locking. Whereas climate dynamics on fast rotating planets is relatively well understood from the Solar system, tidally locked planets still merit more investigations, as we show in this study. Furthermore, slow rotating planets such as Venus show large similarities in climate patterns to tidally locked states (Yang et al. 2014). In addition, planets at the inner edge of the habitable zone are still probably tidally locked, even in the light of the revised tidal theory of Leconte et al. (2015). Incidentally, these planets should be the first to become accessible to atmosphere characterization.

We investigate planets of terrestrial composition, where we assume a bulk density of $\rho_{Earth} = 5.5$ g cm^{-3} for different planet sizes between $R_P = 1$ and $1.45\,R_{Earth}$. As shown in Paper II, the assumption of uniform bulk density makes for easier comparison between radiative and dynamical time-scales and thus easier analysis of atmosphere dynamics evolution with planet size. This assumption yields 1 and 3.1 Earth masses for $R_P = 1$ and $1.45\,R_{Earth}$, respectively.

Table 2. Fixed planetary and atmospheric parameters used in this study.

Parameter	Value
Incident net stellar flux I_{net}	958 W m^{-2}
Obliquity	0°
c_P	1.04 J gK^{-1}
p_s	1000 mbar
Main constituent	N_2
Molecular mass μ	28 g mol^{-1}
Adiabatic index γ	7/5
Rotation period P_{rot}	1–100 d

The rotation period range was selected to cover $P_{rot} = 1$–100 d so that we can compare our results with that of Paper II. The investigated rotation period range is at least down to $P_{rot} = 6.5$ d, relevant for the study of the habitable zone around M dwarf stars (Seager 2013; Zsom et al. 2013). Kaltenegger & Traub (2009) derive $P_{rot} = 2$–65.5 d by taking into account M dwarf host stars down to M9V stars, where the authors assumed a constant planet albedo $\alpha = 0.3$. In Paper II, we derived a relevant orbital period range $P_{orb} = P_{rot} = 2$–90 d for stellar masses $M_* = 0.1$–$0.6\,M_\odot$, for which the Earth equivalent incident flux $I_{net} = I_0(1 - \alpha) = 958$ W m^{-2} reaches the planet. $I_0 = 1368$ W m^{-2} is the incident stellar flux for a given orbital period and $\alpha = 0, 0.3, 0.5, 0.7$ and 0.9 was assumed. Leconte et al. (2013) consider $\alpha = 0.1$–0.5, which corresponds to a relevant orbital period range between $P_{orb} = 6$ and 80 d. Also, Yang, Cowan & Abbot (2013) derive a planetary albedo as high as $\alpha = 0.5$ for tidally locked planets around M dwarfs. Table 2 lists the planetary and atmosphere parameters that we use in this study.

Fast rotation periods ($P_{rot} < 10$ d) allow us, in any case, to study the emergence of dynamical features that are already known from hot Jupiters. The climate state results for these rotation periods are thus a preparation for a more detailed study of climate dynamics on hot Super-Earth planets that lie in the transition region between terrestrial planets and gas giants (Madhusudhan & Redfield 2015).

2.3 Planetary time- and length-scales

The introduction of the following time- and length-scales will be useful in discussing how an increase in nightside cooling efficiency and a change in surface boundary prescription affects the overall climate dynamics evolution for different rotation periods.

The dynamical time-scale t_{dyn} is defined as (Showman, Cho & Menou 2011)

$$t_{dyn} \propto \frac{R_P}{U}, \tag{2}$$

where U is the mean horizontal velocity.

The radiative time-scale used in Papers I and II is

$$t_{rad} = \frac{c_P p_s}{4\, g \sigma T_s^3}, \tag{3}$$

where T_s is the local surface temperature, p_s is the surface pressure and σ is the Stefan–Boltzmann constant. This first-order estimate agrees within one order of magnitude to values derived with full radiative transfer for terrestrial Solar system planets (Paper I).

In Paper II, we confirmed that standing planetary Rossby waves are of uttermost importance for determining climate states of tidally locked planets with rotation periods $P_{rot} = 1$–100 d. More precisely, two types of standing Rossby waves determine which climate state is dominant for specific rotation periods: extratropical and tropical Rossby waves. The former leads to a climate state with high-latitude eastward winds, and the latter leads to the formation of equatorial superrotation.

The possible presence of one or both of these Rossby waves can already be inferred from the calculation of the Rossby radii, where L_R denotes the extratropical Rossby radius and λ_R the tropical Rossby radius (see equations 16 and 17 in Paper II or Holton 1992). We identify atmosphere dynamic transitions with respect to L_R/R_P and λ_R/R_P in Sections 3.4 and 4.2.

For the identification of the precise type of standing Rossby wave, we again use the perturbation method as described in section 4 of Paper II; fig. 2 of that paper depicts the expected perturbations in horizontal wind $\boldsymbol{v}$ and geopotential height $z = \Phi/g$ at the top of

the atmosphere ($p = 225$ mbar) for the tropical and extratropical Rossby waves.

3 NIGHTSIDE COOLING ADJUSTMENT

We found in Paper I that the surface temperatures at the dayside of our nominal model were in good agreement with the Earth climate model of Edson et al. (2011) and Joshi (2003). However, our model's nightside temperatures were about 100 K warmer. We speculated in Paper I that the nightside surface temperatures are mainly determined in our model by the nightside cooling efficiency. In the following, we test this hypothesis. We vary the nightside cooling efficiency via the nightside radiative time-scale $t_{\rm rad,NS}$. In addition, we also investigate how changes in optical depth and planet size affect nightside surface temperatures. The results of our experiments are also compared to Joshi et al. (1997), Joshi (2003) and Edson et al. (2011).

We use the maximum and minimum surface temperatures to track changes in the dayside and nightside heating. Surface temperature maxima are always located very close to the substellar point ($\phi = 0^\circ$) in our climate models. Surface temperature minima are always located at the nightside. However, the latter are shifted from the antistellar point at longitude $\phi = -180^\circ$ towards the morning limb, where the displacement increases with faster planet rotation. In the most extreme case, surface temperature minima are located at $\phi = -120^\circ$. See also fig. 4 of Paper I for surface temperature distributions.

3.1 Radiative efficiency at the nightside

As outlined in Paper I, we use Newtonian cooling for the temperature forcing in our model,

$$\mathcal{F}_T = \frac{T - T_{\rm eq}}{t_{\rm rad}}, \tag{4}$$

where $t_{\rm rad}$ is the radiative time-scale as described in Section 2. The equilibrium temperature $T_{\rm eq}$ is described in detail in Paper I, where we have developed separate prescriptions for the dayside and the nightside. The illuminated dayside is driven towards radiative-convective temperature profiles suitable for a greenhouse atmosphere. The nightside temperature relaxes towards the Clausius–Clayperon relation of the main constituent of the atmosphere (nitrogen).

In the first set of simulations (Exp.1), we take the nominal model as introduced in Paper I as a starting point (Nom.1). Keeping all other parameters equal, the nightside radiative time-scale is successively lowered from $t_{\rm rad,NS} = 813$ d to $t_{\rm rad,NS} = 100$ d (Table 3).

Table 3. Parameters of the experiments used to adjust nightside cooling.

Parameter	Nom.1	Exp.1	Exp.2	Nom.2	Exp.3	Exp.4
$R_{\rm P}$ ($R_{\rm Earth}$)	1.45	1.45	1.45	1	1	1
g (m s^{-2})	14.3	14.3	14.3	9.8	9.8	9.8
$\tau_{\rm s}$	0.62	0.62	0.94	0.62	0.94	0.94
α	0.3	0.3	0.3	0.3	0.3	0.3
$T_{\rm s,max}$ (K)	408	408	425.5	408	425.5	425.5
$t_{\rm rad,DS}$ (d)[a]	5.4[b]	5.4	4.8	8	4.8	3.3
$t_{\rm rad,NS}$ (d)	813	813–100	100	1186[c]	100	69

Notes. [a]$t_{\rm rad,DS}$ is the maximum value at the substellar point.
[b]Note that in Paper I this value was given erroneously as 13 d.
[c]As discussed in Paper II.

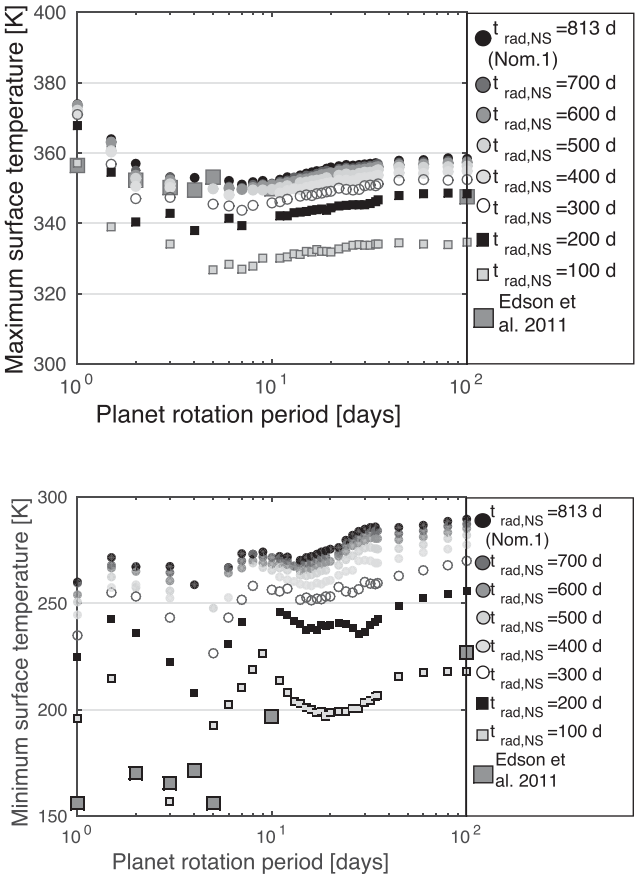

Figure 1. Comparison between maximum (top) and minimum surface temperatures (bottom) in Nom.1 and Exp.1 for different nightside cooling time-scales $t_{\rm rad,NS}$. For comparison, the surface temperatures reported by Edson et al. (2011) are shown.

Fig. 1 shows that just reducing the nightside radiative time-scale to $t_{\rm rad,NS} = 100$ d, reduces the surface temperatures at the nightside by about 80–100 K. The dayside surface temperatures also cool down but to a much lesser degree – by just 25 K compared to the nominal model (Nom.1). Furthermore, Exp.1 with $t_{\rm rad,NS} = 100$ d shows good agreement with nightside temperatures from the dry model of Edson et al. (2011) in the slow rotation regime $P_{\rm rot} \geq 4$ d. The dayside temperatures are colder by 10–20 K.

In the fast rotation regime with $P_{\rm rot} \leq 4$ d, the comparison in surface temperatures between our model and other models is confounded by different possible climate states, as demonstrated in Paper II. Whereas the model of Edson et al. (2011) assumes a climate state with two high-latitude westerly wind jets due to the dominance of a standing extratropical Rossby wave, our model adopts a climate state with a single equatorial superrotating jet due to the dominance of the standing tropical Rossby wave. The latter state suppresses at least the meridional part of the equatorial direct circulation cell and thus suppresses efficient cooling of the substellar point via upwelling. The suppression of equatorial circulation in Exp.1 and Nom.1 leads to very warm substellar point temperatures for very short rotation periods $P_{\rm rot} \leq 4$ d, in contrast to the model used by Edson et al. (2011) who assume colder dayside temperatures due to unperturbed direct circulation.

Despite stronger suppression of direct circulation for faster rotation in the $P_{\rm rot} \leq 4$ d regime, the nightside surface temperature in Exp.1 increases with faster rotation. As outlined in Paper II,

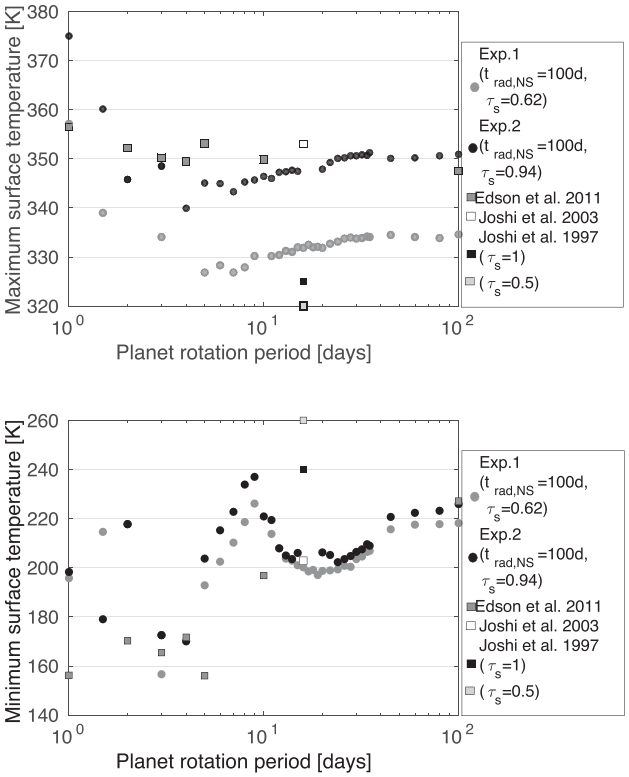

Figure 2. Comparison between maximum (top) and minimum (bottom) surface temperatures in experiments with different optical depths (Exp.1 and Exp.2). For comparison, surface temperatures reported by Edson et al. (2011), Joshi (2003) and Joshi et al. (1997) are shown.

the rise in nightside surface temperatures with faster rotation is attributed to the increasing strength of the secondary circulation cells that transfer heat efficiently from the dayside towards the nightside surface.

In general, we can confirm that it is indeed mainly the nightside cooling efficiency that determines nightside surface temperatures in our simplified model prescription. At the same time, a reduction in $t_{\rm rad,NS}$ affects the dayside surface temperatures only moderately and apparently does not change climate states compared to Nom.1 (discussed in Paper II).

3.2 Adjustment for differences in optical depth

Another complication that arises when comparing different climate models is the differences in optical depth, even assuming the same atmosphere composition. More precisely, $\tau_{\rm s} = 0.62$ was assumed in our nominal model and Exp.1. Edson et al. (2011) adopt $\tau_{\rm s} = 0.94$ (their table 4). To investigate changes in optical depth, we performed another experiment (Exp.2) with $t_{\rm rad,NS} = 100$ d but with dayside equilibrium temperatures calculated for $\tau_{\rm s} = 0.94$ (Table 3).

Fig. 2 shows that an increase in optical depth leads to higher dayside surface temperatures, while the nightside remains virtually unaffected. The surface temperature dependences with optical depth in our prescription as demonstrated by Exp.2 are very different to the results reported by Joshi et al. (1997), who performed similar experiments by changing optical depth between $\tau_{\rm s} = 0.25$ and 2, where only results for 0.5 and 1 are compared in this study. The change in optical depth there led to hardly any changes in dayside surface temperatures but instead affected the nightside temperatures very strongly.

Table 4. Vertical diffusion time-scales of the experiments used to adjust nightside cooling.

$t_{\rm vds}$ (d)	$P_{\rm rot}$ (d)
1	10–100
1 for Nom.1, Nom.2, Exp.1, Exp.3 0.8 for others	9–4
1 for Nom.1, Nom.2, Exp.1 0.8 for others	3–1.5
1 for Nom.1, Nom.2, Exp.1 0.5 for Exp.2 0.2 for Exp.3 0.1 for Exp.4	1

In addition, we find that the stronger heating of the dayside surface in our experiments with higher optical depth (Exp.2, Exp.3 and Exp.4) triggers very strong upwelling over the substellar point. The stronger upwelling leads to violation of static stability for short rotation periods ($P_{\rm rot} \leq 9$ d), if the nominal dry adiabatic adjustment time-scale $\tau_{\rm vds} = 1$ d is used (Section 2.1). When a simulation showed instability, we reduced the diffusion time-scale $\tau_{\rm vds}$ in 0.1-s steps, until static stability could be established again. We find that Exp.4 with strong nightside cooling requires generally the smallest $t_{\rm vds}$ in the short rotation regime. Thus, we justify dry adiabatic adjustment with shorter diffusion time-scale as a parametrization of more vigorous upwelling, which is the strongest for Exp.4. The necessary adjustments in vertical diffusion time-scales $t_{\rm vds}$ are listed in Table 4.

3.3 Adjustment for planet size

Up to now, we have investigated nightside cooling variations for terrestrial-like atmosphere on a tidally locked Super-Earth planet with radius $R_{\rm P} = 1.45\,R_{\rm Earth}$ (Exp.1 and Exp.2). However, many other tidally locked Earth climate models assume $R_{\rm P} = 1\,R_{\rm Earth}$, such as, for example, Edson et al. (2011), Joshi et al. (1997) and Joshi (2003). It was shown in Paper II that just changing the planet size within our model formulation leads to changes in the gradient between dayside to nightside surface temperatures. These changes in planet size were connected to the change in dynamical time-scale $t_{\rm dyn}$, where $t_{\rm dyn} \propto R_{\rm P}$ (equation 2). In Paper II, however, the radiative time-scales $t_{\rm rad}$ also changed via surface gravity g (equation 3): $t_{\rm rad}$ was increased with decreasing planet size. This nominal experiment for an Earth-size planet without increased nightside cooling efficiency (Nom.2) was investigated in detail in Paper II. The corresponding parameters are shown in Table 3.

For Exp.3, we reduce the planet size compared to Exp.2, but keep $\tau_{\rm rad}$ unchanged in contrast to Paper II. That is, we adopt $R_{\rm P} = 1 R_{\rm Earth}$ and $g = 9.8\,{\rm m\,s^{-2}}$ with the same radiative time-scales as in Exp.2. Any changes that arise between Exp.2 and Exp.3 can be therefore exclusively linked to changes in the dynamical time-scale $t_{\rm dyn}$ with reduced planet size.

Fig. 3 shows that just reducing the planet size (keeping all other parameters equal) leads to a decrease in surface temperature dayside to nightside gradient compared to Exp.2. In particular, the nightside temperatures are substantially higher in Exp.3. This result is in accordance with Paper II, where it was likewise found that the gradient between nightside to dayside becomes smaller for smaller planet sizes. In Paper II, this effect was attributed to the combined effect of a decrease in dynamical time-scale $\tau_{\rm dyn}$ and an increase in radiative time-scale. In other words, we have concluded

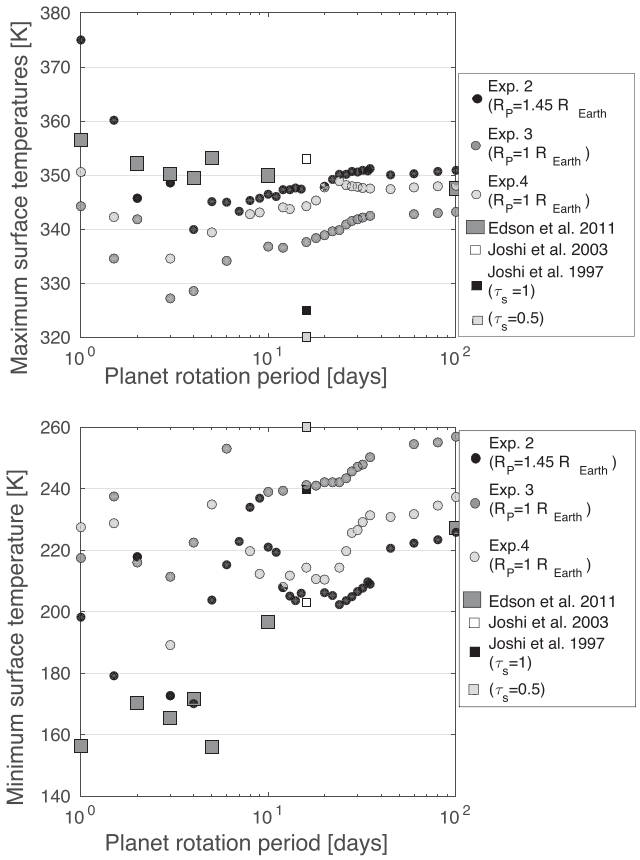

Figure 3. Maximum (top) and minimum (bottom) surface temperatures in Exp.2, Exp.3 and Exp.4, which show adjustment in $t_{\rm rad}$ to compensate for increase in dynamics, when changing the planet size from $R_{\rm P} = 1.45\,R_{\rm Earth}$ to $R_{\rm P} = 1\,R_{\rm Earth}$. In addition, surface temperatures reported by Edson et al. (2011), Joshi (2003) and Joshi et al. (1997) are shown for comparison.

that dynamics becomes more efficient on smaller planets, whereas radiative heating becomes weaker.

As in Paper II, we now assume that dynamics – in the form of flow from the dayside towards the nightside and vice versa – is mainly driven by temperature gradient between the dayside and nightside, which in turn is maintained by radiative heating rate J, the efficiency of which is prescribed in our simplified forcing via $t_{\rm rad}$,

$$J = \frac{\Delta\theta}{t_{\rm rad}}, \tag{5}$$

where $\Delta\theta$ is the difference between the prescribed potential equilibrium temperature and the atmosphere potential temperature. Applying scale analysis on the thermodynamic energy equation (as in Paper II, section 5.1.1), the radiative heating rate J can be linked to dynamics via

$$\frac{\theta U}{R_{\rm P}} \sim \frac{J}{c_{\rm P}}, \tag{6}$$

where, in the context of tidally locked terrestrial planets, $\theta(x, y)$ is the actual difference between dayside to nightside temperatures. Inserting equation (2), we can link $t_{\rm dyn}$ to heating rate and thus $t_{\rm rad}$ via

$$J \sim \frac{\theta}{t_{\rm dyn}}. \tag{7}$$

Because the heating rate J did not substantially change between Exp.2 and Exp.3, we assume that differences in θ are mainly driven by $t_{\rm dyn}$. Furthermore, we assume that we can adjust the heating rate J via $t_{\rm rad}$ to compensate for the more efficient dynamics, increasing the temperature gradient between dayside and nightside again. We decrease $t_{\rm rad}$ at the dayside and nightside by a factor of 1.45 (Table 3) to compensate for changes in $t_{\rm dyn}$ (Exp.4). Exp.4 implies that $t_{\rm dyn} \propto R_{\rm P}$ and that U is, to first order, constant between Exp.3 and Exp.4. Fig. 3 shows that these assumptions are apparently valid. The surface temperatures of Exp.4 are in better agreement with Exp.2 than Exp.3. This relative agreement is particularly evident in the slow rotation regime $P_{\rm rot} \geq 10$ d.

The climate states did not change between Exp.2 and Exp.4, even in the short planet rotation period regime $P_{\rm rot} = 1$–3 d, where we notice the strongest deviations between our nominal model and other tidally locked Earth models, such as Edson et al. (2011) (see Paper II).

It was shown in Paper II that the latter deviations arise because three climate states are possible for $P_{\rm rot} \leq 3$ d on an Earth-size planet: one dominated by standing tropical Rossby waves leading to fast equatorial superrotation, one dominated by extratropical Rossby waves and high-latitude westerly jets and one mixed climate state with contributions from both the tropical and extratropical Rossby waves and thus a mixture between high-latitude westerly jet with equatorial superrotation. The first climate state with pure equatorial superrotation leads to inefficient cooling of the substellar point in contrast to the other two climate states. Its presence can thus already be inferred from dayside surface temperatures that rise steeply with faster rotation. This climate state is apparently adopted by Exp.2, Exp.3 and Exp.4 for $P_{\rm rot} = 1$–3 d (Fig. 3).

Thus, Exp.3 and Exp.4 deviate from the climate states of the corresponding nominal model Nom.2 in the fast rotation regime. It was found in Paper II that the smallest investigated planets ($R_{\rm P} = 1$–$1.25 R_{\rm Earth}$), including Nom.2, show climate states with strong contribution of the extratropical Rossby wave with high-latitude wind jets and only weak or no equatorial superrotation. The efficient nightside cooling in Exp.3 and Exp.4 favours the formation of standing tropical Rossby waves in our model prescription.

Using Exp.4, we can also now more coherently compare surface temperatures arising from our model prescription with increased nightside cooling efficiency with other tidally locked terrestrial climate models. For $P_{\rm rot} = 10$–100 d, Exp.4 agrees with the results of Edson et al. (2011) and Joshi (2003) within 20 K for both the dayside and the nightside (Fig. 3). However, there are large deviations between Exp.4 and Joshi et al. (1997): the dayside surface temperatures are higher by 25–30 K in the former compared to the latter, and the nightside surface temperatures are 30–50 K lower in Exp.4 compared to Joshi et al. (1997).

For $P_{\rm rot} = 4$–10 d, the agreement between surface temperatures at the nightside between Exp.4 and Edson et al. (2011) is less good. Exp.4 is generally warmer by 30–80 K than the dry model of Edson et al. (2011). However, this deviation is small compared to the 100-K difference between Edson et al. (2011) and our nominal model (see Papers I and II). For even faster rotations ($P_{\rm rot} \leq 4$ d), deviations in the dayside surface temperatures arise because Exp.4 and the model of Edson et al. (2011) are in different climate states. The short rotation period simulations shown by Edson et al. (2011) are in climate states dominated by standing extratropical Rossby waves with high-latitude westerly jets and efficient direct circulation even for $P_{\rm rot} = 1$ d (see also Paper II). The efficient direct circulation in the simulations of Edson et al. (2011) prevents the substellar point from reaching surface temperatures hotter than 360 K, even when $P_{\rm rot} = 1$ d (Fig. 3).

It is striking that despite better agreement in surface temperatures between Exp.4 and the model of Edson et al. (2011), compared to the nominal model (Nom.2), the disagreement between climate states in the short rotation period regime is even stronger. While Nom.2 exhibited – at least sometimes – standing extratropical Rossby waves for $P_{\rm rot} \leq 3$ d, like the model of Edson et al. (2011), these tendencies disappear in Exp.4 with stronger nightside cooling. Apparently, tropical Rossby waves become stronger when the thermal forcing increases in our model, and they dominate in Exp.4 for all rotation periods.

The comparison between experiments with efficient and inefficient nightside cooling and with other climate models in the fast planet rotation regime demonstrates an important principle. It is vital first to understand the possible basic climate states arising from 3D climate models, before attempting to compare their details with each other.

3.4 Effect of increased nightside cooling efficiency on large-scale climate dynamics

Up to now, we have only inspected the evolution of surface temperatures between $P_{\rm rot} = 1$ and 100 d. Based on this evolution, we have already concluded that an increase in nightside cooling efficiency not only leads to a strong cooling of the nightside, but also favours more strongly the formation of tropical Rossby waves, even for small planets ($R_{\rm P} = 1\,R_{\rm Earth}$) and fast planet rotations ($P_{\rm rot} \leq 3$ d).

In the following, we aim to confirm the conclusion that climate states brought upon by standing tropical Rossby waves are more prevalent in simulations with efficient nightside cooling, represented by Exp.4, compared to the nominal model (Nom.2). For this purpose, we investigate the evolution of climate states for $P_{\rm rot} = 1$–100 d by consulting additional diagnostics: the evolution of zonal wind versus rotation period, Rossby wavenumbers and circulation patterns. We discuss deviations from climate states compared to Nom.2 that are described in detail in Paper II.

3.4.1 Zonal wind

The inspection of the maximum zonal wind speeds versus planet rotation periods is a good starting point to discuss climate dynamics in a large parameter study as demonstrated in Paper II and Edson et al. (2011). In this study, we find that wind speeds arising from simulations with increased nightside cooling efficiency (Exp.1 and Exp.4) are generally larger than the respective nominal simulations with less efficient nightside cooling (Nom.1 and Nom.2) (see Fig. 4). The larger wind speeds arise because Exp.1 and Exp.4 have smaller radiative time-scales, increasing the heating rate via $J \propto t_{\rm rad}^{-1}$, which triggers faster winds.

For faster planet rotations ($P_{\rm rot} \leq 3$ d), Exp.1 and Exp.4 exhibit fast equatorial superrotation, whereas Nom.2 shows climate states with high-latitude wind jets or at least a mixed state for $P_{\rm rot} =$ 1.5, 2 and 3 d, with both equatorial superrotation and high-latitude wind speeds existing side by side (Paper II). High-latitude jets have much slower wind speeds than those of superrotating equatorial jets, which explains why Nom.2 has slower wind speeds in the short planet rotation regime compared to Exp.4 (Fig. 4). Thus, the zonal wind evolution confirms that more efficient nightside cooling in our model prescription, and thus stronger thermal forcing, suppresses the formation of standing extratropical Rossby waves and also the formation of high-latitude wind jets for small exoplanets.

Interestingly, Exp.4 yields zonal wind speeds in the intermediate and slow rotation period range $P_{\rm rot} = 4$–100 d comparable to those

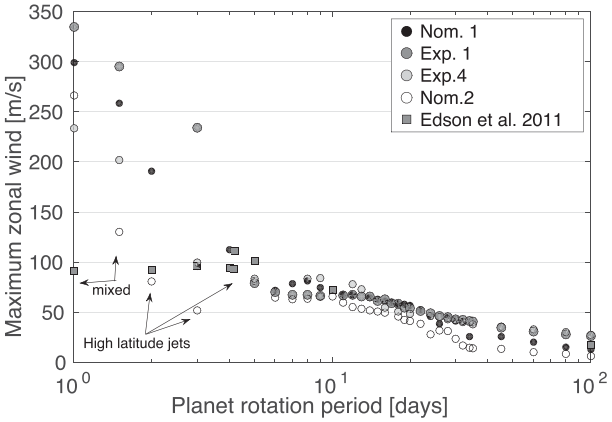

Figure 4. Maximum of zonal wind speeds in our model with efficient and inefficient nightside cooling, different optical depths and planetary radii and as reported by Edson et al. (2011) in their model.

reported by Edson et al. (2011) (Fig. 4). Exp.4 assumes the same optical depth and planet size as the dry climate model used by Edson et al. (2011). This agreement indicates that the thermal forcing between Exp.4 and the model used by Edson et al. (2011) are of similar strength. The similarity in thermal forcing was already inferred in the previous section by similar gradients in the dayside to nightside surface temperatures. This result confirms once again that the climate states arising in the fast rotation regime can be very different, despite similar strength in thermal forcing between Exp.4 and the model of Edson et al. (2011).

As reported in Paper II, there are distinct phase changes in climate states for planet rotation periods between 1 and 100 d that can be linked to the tropical and extratropical Rossby radii of deformation over planet size, $\lambda_{\rm R}/R_{\rm P}$ and $L_{\rm R}/R_{\rm P}$, respectively. Fig. 5 shows that all climate state transitions connected to the tropical and extratropical Rossby wave are shifted slightly towards faster planet rotation for Exp.4 compared to Nom.2. The climate states concerned are those for which either the tropical or the extratropical Rossby wave becomes smaller than the planetary radius ($\lambda_{\rm R}/R_{\rm P} \leq 1$ and $L_{\rm R}/R_{\rm P} \leq 1$, respectively) and those for which either the tropical or extratropical Rossby wave becomes smaller than half the planetary radius ($\lambda_{\rm R}/R_{\rm P} \leq 0.5$ and $L_{\rm R}/R_{\rm P} \leq 0.5$, respectively). Closer inspection (not shown) shows that the shift is due to an increase in scaleheight H of Exp.4 compared to Nom.2 because of the higher average surface temperatures.

We now monitor the presence of planetary waves for different climate states with respect to the tropical and extratropical Rossby radii over planet size:

(i) $\lambda_{\rm R}/R_{\rm P} > 1$;
(ii) $\lambda_{\rm R}/R_{\rm P} \approx 1$;
(iii) $L_{\rm R}/R_{\rm P} \leq 1$ and $\lambda_{\rm R}/R_{\rm P} \leq 0.5$;
(iv) $L_{\rm R}/R_{\rm P} \leq 0.5$.

For this purpose, we use the perturbation method and inspect the eddy geopotential height z' and the eddy horizontal wind velocity v' on top of the atmosphere ($p = 225$ mbar) for planet rotation periods around the relevant Rossby wavenumbers.

3.4.2 Slow rotations with $\lambda_{\rm R}/R_{\rm P} > 1$

Interestingly, we find that even for the slowest rotator with $P_{\rm rot} =$ 100 d, there are changes in climate dynamics. Exp.4 is no longer exclusively dominated by direct divergent flow from the substellar

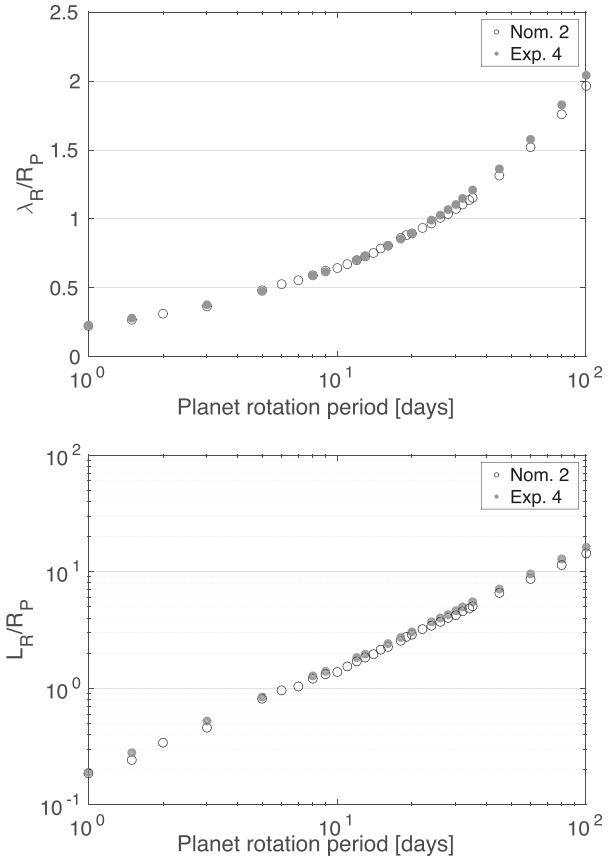

Figure 5. Tropical Rossby radius of deformation λ_R (top) and extratropical Rossby radius of deformation over planet size $R_P = 1\,R_{Earth}$ (bottom) for Exp.4 and Nom.2.

point towards the nightside in contrast to Nom.2 (Paper II). Divergent flow is still the main feature in this rotation regime as evidenced by the positive geopotential perturbation associated with divergent flow over the substellar point (Fig. 6, top). This flow leads, as described in Paper II, to relative cold upper atmosphere temperatures (Fig. 6, bottom). However, in addition, two cyclones with local temperature maxima on the north-west and south-west flank of the substellar point (longitude $\phi = -90^\circ$) are visible (Fig. 6, top and bottom). These cyclones are associated with negative geopotential perturbations between latitudes $\pm 50^\circ$.

Geopotential perturbations at the equator are the hallmark of a Kelvin wave (Matsuno 1966). The two cyclones and the east–west asymmetry in eddy geopotential height and flow was also observed around the Kelvin wave by Gill (1980). At the same time, it appears that the negative geopotential height perturbation at the equator ($\phi = -90^\circ$) is superimposed by two negative geopotential perturbations with Rossby wave gyres centred at latitudes $\pm 40^\circ$ (see also the bottom panel of fig. 2 in Paper II). Shear between Kelvin waves and tropical Rossby waves typically causes equatorial superrotation, which is indeed observed in Exp.4 (Fig. 6, middle panel).

The presence of a stronger Kelvin wave compared to the nominal model Nom.2 can be explained by the stronger thermal forcing. Kelvin waves are associated with longitudinally varying heating patterns and we increased the temperature difference between dayside and nightside in Exp.4 compared to Nom.2. However, the dry model of Edson et al. (2011) shows purely divergent flow for $P_{rot} = 100$ d without any indication of Kelvin waves, even though their model has similar strength in thermal forcing than Exp.4. Thus,

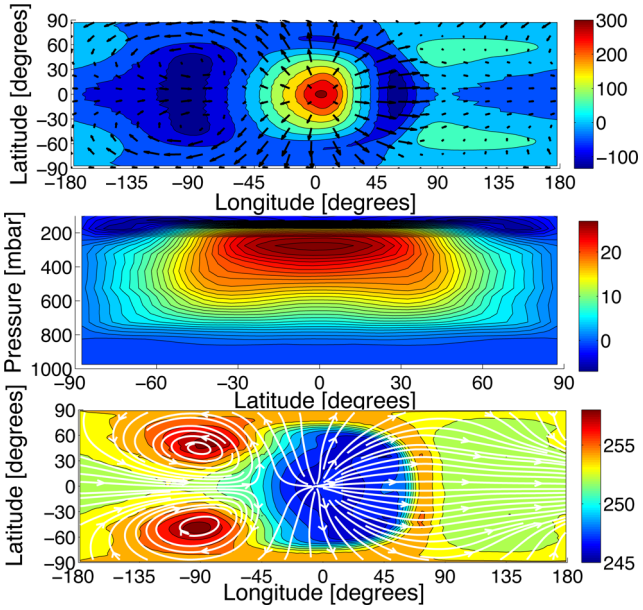

Figure 6. The climate state of the $P_{rot} = 100$ d simulation for Exp.4. Top: eddy geopotential height in m and eddy horizontal wind in m s^{-1} at $p = 225$ mbar. Middle: zonal mean of the zonal flow in m s^{-1}. Bottom: temperatures (contour interval 1 K) and streamlines of the horizontal flow at $p = 225$ mbar. The longest eddy wind vectors are 64.6 m s^{-1}. Contour intervals are 50 m for the eddy geopotential and 1 m s^{-1} for zonal winds.

we conclude that strong thermal forcing is one, but not the sole, factor that can trigger Kelvin waves even for slow planet rotation.

However, the appearance of tropical Rossby gyres in Exp.4 already for $P_{rot} = 100$ d is puzzling. We have found, in Paper II, the formation of tropical Rossby waves only for $\lambda_R/R_P \leq 1$. Here, $P_{rot} = 100$ d corresponds to $\lambda_R/R_P = 2$ (Fig. 5). Just based on the tropical Rossby radius of deformation, we would not expect standing Rossby waves.

The Rossby wave, however, can only be weak: equatorial superrotation in Exp.4 for $P_{rot} = 100$ d is relative slow (≈ 25 m s^{-1}). Therefore, the horizontal flow in the upper atmosphere is still largely dominated by direct divergent flow as evidenced by the velocity streamlines in the upper atmosphere (Fig. 6, middle). The corresponding geopotential height anomalies associated with possible Rossby wave gyres are also much smaller than the positive geopotential perturbation over the substellar point associated with the hot substellar point (Fig. 6, top). Thus, we conclude that the additional appearance of weak Kelvin and Rossby waves has, in this specific example, only a minor influence. Direct divergent flow still dominates in this slow rotation regime, as expected. We can conclude that Exp.4 shows not only a stronger tendency to form tropical Rossby waves in the short rotation period but also, surprisingly, in the long rotation period regime ($P_{rot} = 100$ d) compared to Nom.2.

3.4.3 *Intermediate rotations with $\lambda_R/R_P \approx 1$*

The climate state transition at $\lambda_R/R_P \approx 1$ towards atmosphere dynamics with a standing tropical Rossby wave was identified in Paper II with the emergence of geopotential height anomalies away from the equator (see the bottom panel of fig. 1 in Paper II). While this transition is straightforward and easy to identify for models that are exclusively dominated by direct circulation flow in the slow

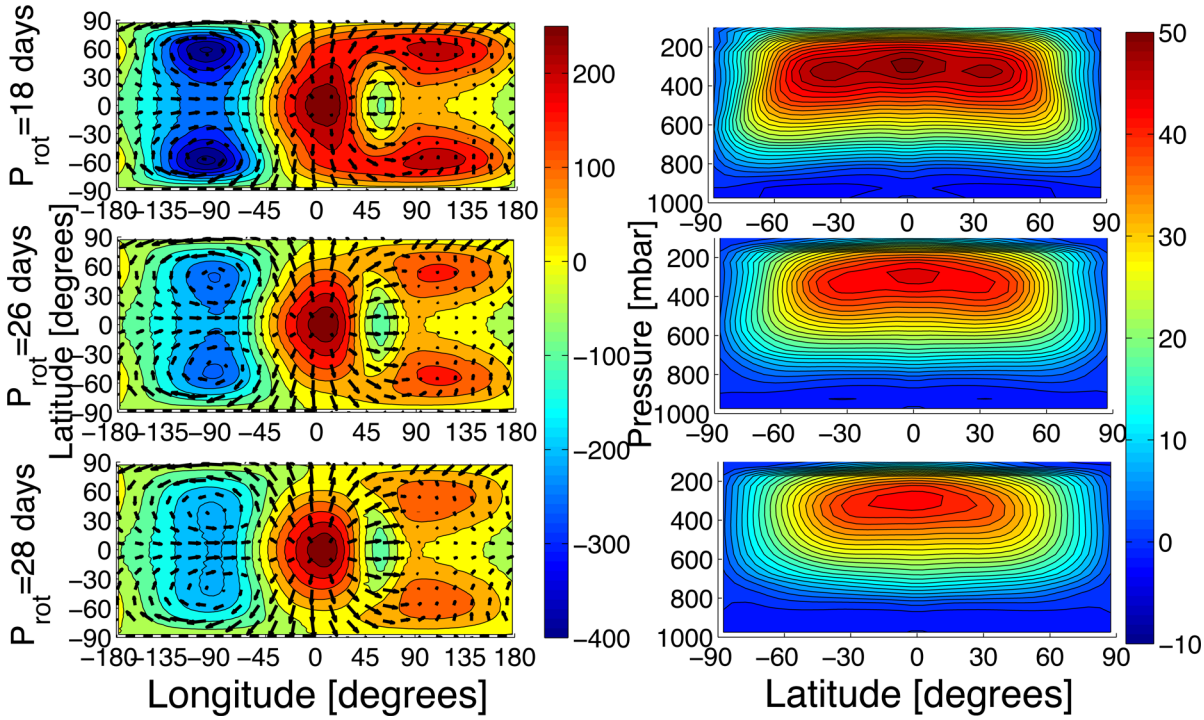

Figure 7. The climate state transition, $\lambda_R/R_P \approx 1$, and Exp.4 for $P_{rot} = 18$, 26 and 28 d (from top to bottom). Left: eddy geopotential height in m and eddy horizontal wind in m s^{-1} at $p = 225$ mbar. Right: zonal mean of the zonal flow in m s^{-1}. The longest eddy wind vectors are from top to bottom 64.3, 64.0 and 56.1 m s^{-1}, respectively. Contour intervals are 50 m for the eddy geopotential and 2 m s^{-1} for zonal wind speeds, respectively.

rotation regime (Nom.2), it is interesting to observe what happens in Exp.4.

While weak Rossby waves are already present for relative slow rotations in Exp.4 (see previous section), the waves only fully form when the tropical Rossby wavenumber becomes smaller than unity. The transition to a climate state that is dominated by standing tropical Rossby waves can be identified with two distinct negative geopotential perturbations at longitude $\phi = -90$ and latitudes $\nu = \pm 60$. These start to form two distinct gyres for $P_{rot} = 26$ d and faster rotations. This transition occurs indeed at $\lambda_R/R_P = 1$ (Fig. 5). Furthermore, the formation of Rossby wave gyres leads to an increase in equatorial wind speeds with faster and faster rotation (Fig. 7, right panel at $p = 300$ mbar). The full formation of standing tropical Rossby waves in the expected rotation regime confirms that the planetary waves reported in the previous section can only be weak.

3.4.4 Climate state bifurcation I: $L_R/R_P \leq 1$ and $\lambda_R/R_P \leq 0.5$

As reported in Paper II, the transition in extratropical Rossby waves via $L_R/R_P \leq 1$ and in tropical Rossby waves via $\lambda_R/R_P \leq 0.5$ can occur roughly at the same rotation period. That is, $P_{rot} = 6$ d for Exp.4 and Nom.2. Therefore, we can expect either the strengthening of standing tropical Rossby waves with faster rotation between $P_{rot} = 10$ and 4 d, or we can expect an abrupt transition to another climate state dominated by standing extratropical Rossby waves. As reported by Paper II, the maxima of zonal wind speeds decrease abruptly with faster rotations at $L_R/R_P \approx 1$, when standing extratropical Rossby waves form.

A drop in maximum zonal wind speed with faster rotation can indeed be seen for Nom.2 and $P_{rot} = 5$ d (Fig. 4). Closer inspection of flow patterns (not shown) does reveal a transition from a climate state with equatorial superrotation to a new climate state with two high-latitude wind jets (see Paper II). However, Exp.4 assumes a climate state dominated by equatorial superrotation for the whole investigated rotation regime, as evidenced by the smooth increase in zonal wind speeds with faster rotations from $P_{rot} = 100$ d to $P_{rot} = 1$ d (Fig. 4).

Thus, we conclude that more efficient nightside cooling leads, via the larger dayside to nightside temperature gradient, to a dominance of standing tropical Rossby waves also for small exoplanets with $R_P = 1\,R_{Earth}$. In contrast to that, weaker thermal forcing (Nom.2) allows for the formation of standing extratropical waves. The emergence of faster equatorial superrotation (tropical Rossby waves) compared to the slower high-latitude jets (extratropical Rossby waves) explains why Exp.4 has higher zonal wind speeds than Nom.2 for rotation periods $P_{rot} \leq 6$ d.

3.4.5 Climate state bifurcation II: $L_R/R_P \leq 0.5$

For even faster rotations, the extratropical Rossby wave has another possible transition, when $L_R/R_P \leq 0.5$. This is at $P_{rot} = 3$ d for Exp.4. In this rotation regime, the tropical and extratropical Rossby waves can both fit on the planet allowing for mixed states with combined tropical and extratropical Rossby waves. Indeed, mixed states can be found for Nom.2 in the expected rotation regime (Fig. 4, arrows indicating mixed states). For $P_{rot} = 1$ d, however, Nom.2 goes again into full equatorial superrotation, which can be seen by the very fast zonal wind speeds of $u = 275$ m s^{-1} that the model assumes (Fig. 4 at $P_{rot} = 1$ d). Different possible climate states for the fast rotation regime also explain why surface temperatures, in particular at the nightside, can vary so strongly between different models with rotations faster than $P_{rot} = 10$ d (Fig. 3).

We concluded in Paper II that the tropical Rossby wave is stronger in Nom.2 than in the model used by Edson et al. (2011), where

extratropical Rossby waves dominate even for very fast rotations $P_{\rm rot} = 1$ d. We find that the model with more efficient nightside cooling (Exp.4) is even more strongly dominated by the tropical Rossby wave in the short-period and also in the long-period rotation regime. Stronger thermal forcing via efficient nightside cooling favours formation of standing tropical Rossby waves. This result is not entirely unexpected, because one of the driving mechanisms for superrotation is longitudinal heating differences in the form of the dayside to nightside temperature gradient that trigger the formation of Kelvin waves (Showman & Polvani 2011).

This point is still worthwhile emphasizing, because the comparison between our nominal model with the model of Edson et al. (2011) yielded the comparatively warm nightside surface temperatures as one possible source of deviation. Therefore, one might suspect that stronger thermal forcing might lead to climate states dominated by extratropical Rossby waves, as demonstrated by the model of Edson et al. (2011). Exp.4 has shown that stronger thermal forcing alone in fact has the opposite effect.

3.4.6 *Circulation*

The larger dayside to nightside temperature gradient, and thus also pole to equator surface temperature gradient at the dayside[3] in Exp.4 should promote more efficient circulation for the same planet size and rotation period. In the following, we investigate how circulation in Exp.4 changes compared to Nom.2.

We identify circulation states by monitoring the maximum and minimum of the meridional mass transport stream function Ψ. This is defined as

$$\Psi = \frac{2\pi R_{\rm P}}{g} \cos\nu \int_0^p \bar{v}\, {\rm d}p', \tag{8}$$

where ν is latitude and $\bar{v}$ is the zonal and temporal mean of the meridional velocity component v at a given latitude.[4] Ψ is positive for clockwise circulation and negative for counter-clockwise circulation. Thus, the direct circulation cell has positive Ψ and the secondary cell negative Ψ on the Northern hemisphere.

The overall circulation efficiency of the direct equatorial cell is indeed greater for Exp.4 compared to the nominal model (see also Paper II, fig. 17). Thus, the slow rotation regime is generally dominated by two large direct circulation cells (state 0), as expected from previous studies such as Edson et al. (2011) and Navarra & Boccaletti (2002). When Exp.4 reaches the $\lambda_{\rm R}/R_{\rm P} \leq 1$ transition with faster rotation, the circulation evolves into a state with an embedded reverse circulation cell (state 1). The development coincides with a climate state dominated by standing tropical Rossby waves at $P_{\rm rot} = 18$–28 d (Section 3.4.3). In Fig. 8, upper panel, the development of a state 1 circulation can be inferred by the steep drop in direct circulation cell strength with faster rotation at $P_{\rm rot} = 18$ d. The nominal model (Nom.2) forms state 1 for slower rotations at $P_{\rm rot} = 22$ d.

[3] We can use dayside to nightside temperature differences to infer pole to equator differences, because the surface temperatures at the nightside are relatively uniform compared to the dayside. At the nightside, the surface temperature gradient is only about $\Delta T \leq 20$ K. On the dayside, the surface temperature contrast is $\Delta T \geq 60$ K; see also fig. 4 of Paper I or fig. 1 of Merlis & Schneider (2010). Therefore, we can assume to first order that the terminators and the poles are as cold as the nightside.

[4] Note that the horizontal wind velocity is $\boldsymbol{v} = (u, v)$, where u is the zonal and v is the meridional component.

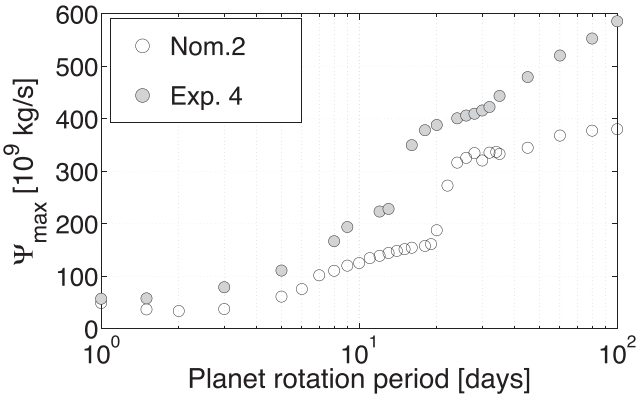

Figure 8. Maxima of the meridional mass transport stream function Ψ on the Northern hemisphere for the direct circulation cell in Nom.2 and Exp.4, both for $R_{\rm P} = 1\, R_{\rm Earth}$.

Table 5. Circulation cells.

$R_{\rm P}$	$P_{\rm rot}$ (d)			
($R_{\rm Earth}$)	State 0	State 1	State 2	State 3
Nom.2	100–22	20–13	12–1.5	1
Exp.4	100–18[a]	17–8	5–3	1.5–1

Note. [a]Here, state 0 contains in this case a weak polar cell.

We attribute the formation of state 1 circulation for faster planet rotation in Exp.4 compared to Nom.2 to the presence of weak Rossby waves that already appear for slow rotations $P_{\rm rot} = 100$ d in Exp.4 (Section 3.4.2). While it was found that the Rossby waves play only a minor role in the slow rotation regime due to their weakness, they are apparently still strong enough to hamper the formation of embedded reverse circulation cells in the intermediate rotation regime. Also, the transition to circulation states with two fully vertical extended circulation cells (state 2) is shifted towards faster rotations in Exp.4 compared to Nom.2 (Table 5).

4 SURFACE FRICTION AND PLANETARY BOUNDARY LAYER VARIATION

In the following, we investigate how climate dynamics changes for variations of the extent of planetary boundary layer (PBL) and the efficiency of surface friction. For these experiments, we use the nominal model (Nom.1) for a Super-Earth planet with $R_{\rm P} = 1.45\, R_{\rm Earth}$ and terrestrial bulk density, as introduced in Paper I, as a basis. See Table 3 for the relevant parameters of Nom.1.

4.1 Rayleigh friction prescription

The Rayleigh friction mechanism prescribed in our model is

$$\boldsymbol{F}_v = -\frac{1}{t_{\rm fric}} \boldsymbol{v}, \tag{9}$$

where $t_{\rm fric}$ is defined as

$$t_{\rm fric} = t_{\rm s,fric} \max\left[0, \frac{(p/p_{\rm s}) - (p_{\rm PBL}/p_{\rm s})}{1 - (p_{\rm PBL}/p_{\rm s})}\right], \tag{10}$$

where $p_{\rm PBL}$ is the pressure at the upper vertical limit of the PBL and $t_{\rm s,fric}$ is the maximum surface friction. For the Earth, $t_{\rm s,fric} = 1$ d and $p_{\rm PBL} = 700$ mbar is assumed (Held & Suarez 1994). However, even for Mars, several models assume that $t_{\rm s,fric}$ and $p_{\rm PBL}$ vary by orders of magnitude (see Paper II for a more detailed discussion). Heng &

Table 6. Parameters of the experiments used to investigate different surface prescriptions.

Parameter	Exp.5	Nom.1	Exp.6	Exp.7	Exp.8	Exp.9	Nom.1
$t_{s,fric}$ (d)	0.1	1	10	100	1	1	1
p_{PBL} (mbar)	700	700	700	700	800	900	700

Vogt (2011) studied variations of $t_{s,fric}$ with four experiments, but did not vary the extent of the PBL and covered only one rotation period: $P_{rot} = 36.5$ d. Furthermore, at the same time they changed radiative forcing and only reported surface temperatures and velocities.

In this study, we use Nom.1 as a basis and keep t_{rad} the same for every experiment in this subsection (Table 3). We study surface friction time-scales for $t_{s,fric} = 0.1$, 1,10 and 100 d and assign for $t_{s,fric} = 1$ d three upper extents of the planet boundary layer: $p_{PBL} = 700$, 800 and 900 mbar (see Table 6). These variations cover the values that were identified in Paper I from climate models of Solar system terrestrial planets. For each scenario, we cover the whole relevant rotation period range $P_{rot} = 1$–100 d to monitor coherently climate dynamics transitions at $\lambda_R/R_P = 1$ and 0.5 and $L_R/R_P = 1$ and 0.5 due to surface boundary variations.

4.2 Effect of surface friction and PBL extent on large-scale dynamics

To roughly identify climate state changes, we monitor again zonal wind speeds, which are defined as positive for westerly winds and negative for easterly winds.

4.2.1 Zonal wind

Fig. 9, upper panel, shows that westerly wind speeds generally increase as surface friction efficiency decreases for fast rotation ($P_{rot} \leq 10$ d) and slow rotations ($P_{rot} \geq 40$ d). For intermediate rotations ($P_{rot} = 10$–40 d), zonal wind speed evolution for different surface friction time-scales is surprisingly complex. For example, we find for $P_{rot} = 10$–20 d that the model with the most efficient surface friction (Exp.5) has strongest westerly winds. In contrast, the model with the least efficient surface friction (Exp.7) has the weakest westerly winds.

Even more surprisingly, Fig. 10 reveals that Exp.7 shows predominantly easterly zonal winds in the slow and intermediate rotation regime ($P_{rot} = 12$–100 d) with relatively high zonal wind speeds for the slow rotation regime: $u = -50$ to $-80\,m\,s^{-1}$. As rotation period decreases, Exp.7 transits into a regime with westerly zonal wind tendency at $P_{rot} = 12$ d (Fig. 10). The transition occurs well in the standing tropical Rossby wave rotation regime ($\lambda_R/R_P < 1$; see Table 7).

Models with weak surface friction may shed light on climate dynamics in the intermediate regime between terrestrial planets and Mini-Neptunes without a solid surface. The latter planets should have weak or no lower boundary friction. Based on the result from this section, we would assume that Mini-Neptunes generally experience faster wind speeds than terrestrial planets for the same thermal forcing. Indeed, tidally locked Mini-Neptune models for GJ1214b ($P_{rot} = 1.58$ d) exhibit fast westerlies with wind speed of up to 2 km s^{-1} (e.g. Menou 2012). However, GJ1214b experiences 16 times the stellar irradiation than the terrestrial planets discussed in this work and is thus not in the same thermal forcing regime (Charbonneau et al. 2009).

The extent of the PBL has also a relatively strong effect on zonal wind speeds, as evidenced in Fig. 9, lower panel. The wind velocities

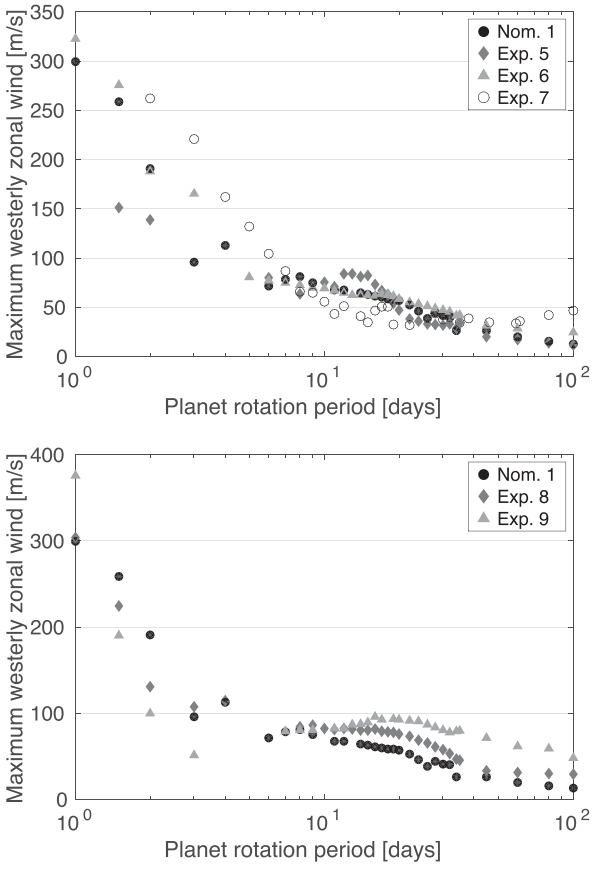

Figure 9. Maximum of westerly wind speeds in m s^{-1} for different surface friction time-scales $t_{s,fric} = 0.1$–100 d (top) and different PBL extent $p_{PBL} = 700$–900 mbar (bottom).

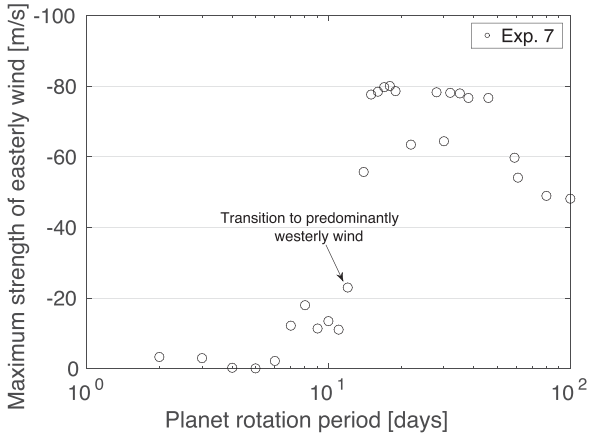

Figure 10. Maximum strength of easterly wind speeds in m s^{-1} for surface friction time-scale $t_{s,fric} = 100$ d and $R_P = 1.45\,R_{Earth}$.

Table 7. Rossby wavenumber transitions for $R_P = 1.45\,R_{Earth}$.

R_P (R_{Earth})	P_{rot} for L_R/R_P ≈0.5 d	≈1 d	P_{rot} for λ_R/R_P ≈1 d	≈0.5 d
1.45	5	10	34	8

are larger for smaller PBL extent in the intermediate and slow rotation regime ($P_{rot} = 10$–100 d). This tendency reverses in the fast rotation regime ($P_{rot} = 1.5$–3 d), where the wind speeds are lower for smaller PBL extent. The fast planet rotation regime ($P_{rot} = 1$–3 d) coincides with the Rossby wave regime $L_R/R_P \leq 0.5$ (see Table 7),[5] where we found in Paper II that standing extratropical Rossby waves can form alongside standing tropical Rossby waves. In Paper II, we also showed that climate states with strong extratropical Rossby waves have lower wind speeds than climate states dominated by tropical Rossby waves that exhibit strong equatorial superrotation. Thus, it appears likely that extratropical Rossby waves form in Exp.9 for fast planet rotation periods based on the displayed low wind speeds. The wind speeds of every model with different PBL extent converge towards full strong equatorial superrotation for very fast planet rotation periods, $P_{rot} = 1$ d, and reach high velocities of $u \approx 300$ m s^{-1}.

In the following, we discuss in more detail differences arising from surface boundary variations at climate state transitions with respect to standing tropical and extratropical Rossby waves as identified in Paper II. The location of transition regions in the rotation period for the set of models investigated in this section are listed in Table 7. We compare the results of Exp.5–9 to the climate states of Nom.1, as reported in Paper II.

4.2.2 *Slow rotations with $\lambda_R/R_P > 1$*

As already shown in the previous section, Exp.7 with very weak surface friction ($t_{s,\,fric} = 100$ d) has predominantly easterly winds in the slow planet rotation regime ($P_{rot} \geq 34$ d). This behaviour is in contrast to all other experiments (Exp.5, Exp.6, Exp.8 and Exp.9) and the nominal model (Nom.1). This is evident in the zonal mean of the flow (Fig. 11, bottom-right) and even in the horizontal flow pattern at $p = 225$ mbar (Fig. 12, bottom-right).

Inspection of the eddy geopotential height and wind reveals very deep negative geopotential height perturbations that are centred at the equator and located east and west of the substellar point between $\phi = -90°$ and $\phi = -180°$ and between $\phi = +90°$ and $\phi = +180°$ (Fig. 13, bottom-right). Furthermore, there are strong easterly eddy winds $\boldsymbol{v}'$ that are confined along the equator between $\phi = -90°$ and $0°$. Interestingly, again two cyclones are present in the horizontal flow in the upper atmosphere. However, the vortices are flipped with respect to their counterparts with normal westerly winds in the same rotation regime but with stronger surface friction (Exp.5, Exp.6, Exp.8 and Nom.1) from $\phi = -135°$ to $\phi = +135°$ (Fig. 12).

The zonal confinement of eddy winds along the equator and deep geopotential anomalies centred over the equator in Exp.7 are indications of a Kelvin wave (Matsuno 1966) that may be triggered by a very cold nightside and thus a strong horizontal temperature gradient. However, Kelvin waves only propagate eastward, which is the reverse direction of the observed zonal winds. The cyclones normally indicate the presence of a large-scale Rossby wave that should propagate in the westerly direction. The shear between Kelvin and Rossby waves should thus lead to a westerly equatorial wind not an easterly (Showman & Polvani 2011). In addition, the slow planet rotation ($P_{rot} = 100$ d) is too slow to elicit a strong Rossby wave. Thus, we are currently at a loss to explain this peculiar easterly flow in Exp.7.

[5] The Rossby radii of deformation are only weakly affected by changes in surface friction and PBL compared to the nominal model.

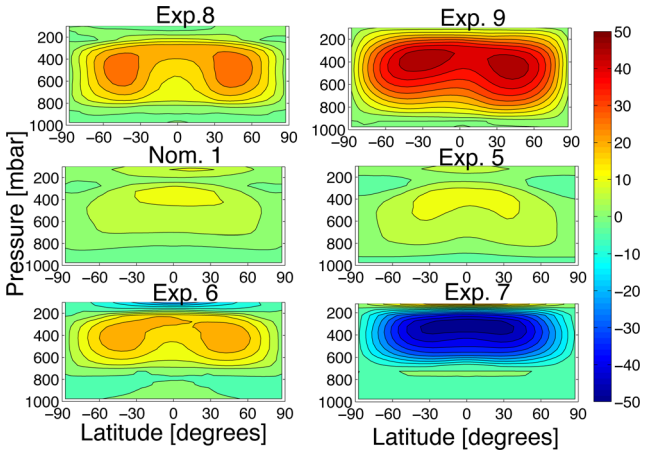

Figure 11. Zonal mean of zonal winds in m s^{-1} for $P_{rot} = 100$ d and Exp.8, Exp.9 and Nom.1, which have varying different PBL extents ($p_{PBL} = 800$, 900 and 700 mbar, respectively) and Exp.5, Exp.6 and Exp.7, which have varying surface friction time-scales ($t_{s,fric} = 0.1$, 10 and 100 d, respectively). Contour levels are 5 m s^{-1}.

In general, we find that the depth of negative geopotential perturbations in the slow rotation regime is larger with less efficient surface friction, as comparison between Exp.6, Exp.7 and Nom.1, in particular, shows (Fig. 13, bottom panels and middle-left panel). The deeper negative geopotential perturbations suggest that the nightside surfaces are comparatively cold in these models. The negative geopotential perturbations z' are connected to cyclones that become stronger with decreasing z'. The stronger vortices result, in turn, in warmer temperature maxima in the upper atmosphere (Fig. 12, bottom panels and middle-left panel) and also in faster zonal wind speeds $|u|$ (Fig. 9, upper panel, and Fig. 10).

Models with more compressed PBL extent (Exp.8 and Exp.9) show signs of additional dynamics apart from direct circulation in the slow planet rotation regime (Fig. 13, top panels). Direct circulation is visible in the eddy geopotential height field as a strong positive geopotential height anomaly over the substellar point that indicates the upwelling branch of direct circulation. Exp.8 and Exp.9 show that negative geopotential height anomalies appear along with weak tropical Rossby wave-like gyres at mid-latitudes $\nu = \pm 60°$ and $\phi = -135°$. These Rossby gyres are particulary evident in Exp.9 (Fig. 13, top-right).

The appearance of these additional dynamical features is surprising, because the $P_{rot} = 100$ d simulations are in a Rossby wavenumber regime with $\lambda_R/R_P > 1$ – more precisely, $\lambda_R/R_P = 1.75$. In the nominal model, standing tropical Rossby wave features were only found for $\lambda_R/R_P \approx 1$ (see Paper II). For larger λ_R/R_P, the Rossby wave should not be able to fit on the planet.

However, Exp.4, with efficient nightside cooling, has already demonstrated that weak tropical Rossby wave-like gyres can form for $P_{rot} = 100$ d (Section 3.4.2). It was further shown in Section 3.4.3 that Exp.4 only assumes a climate state dominated by standing tropical Rossby waves, if $\lambda_R/R_P < 1$, as expected from Paper II. The evidence of Rossby waves in Exp.8 and Exp.9 confirms our

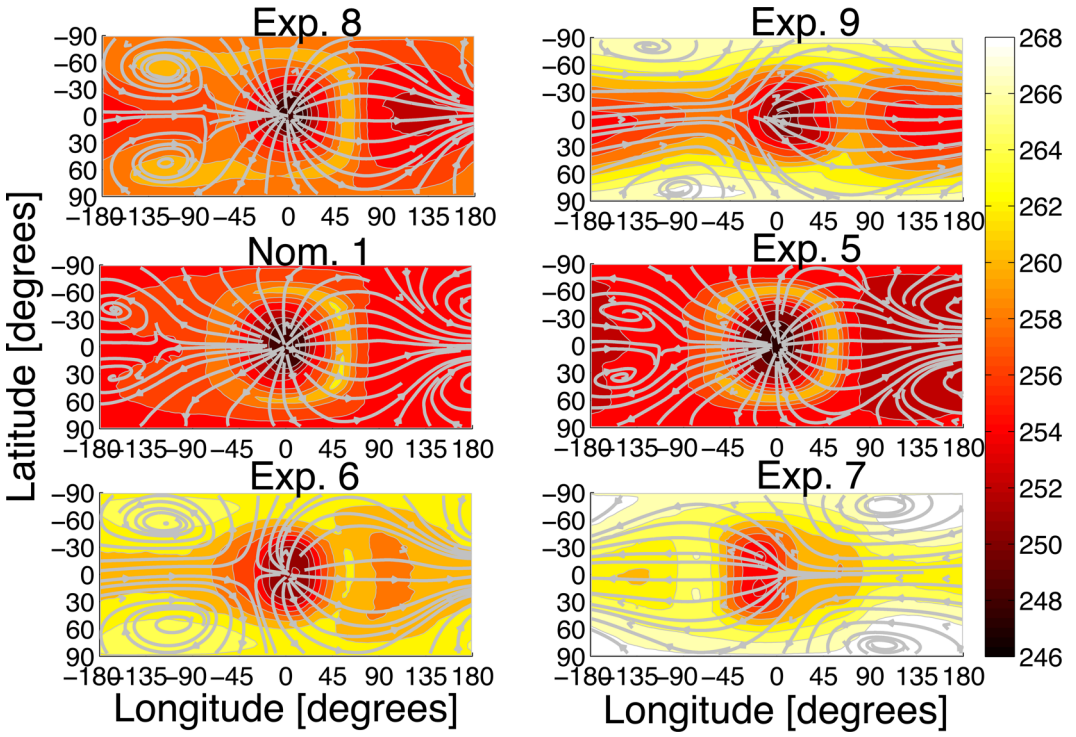

Figure 12. Temperatures (contour interval 2 K) and streamlines of the horizontal flow at $p = 225$ mbar for the $P_{\rm rot} = 100$ d simulation of Exp.8 and Exp.9, the nominal model and Exp.5, Exp.6 and Exp.7.

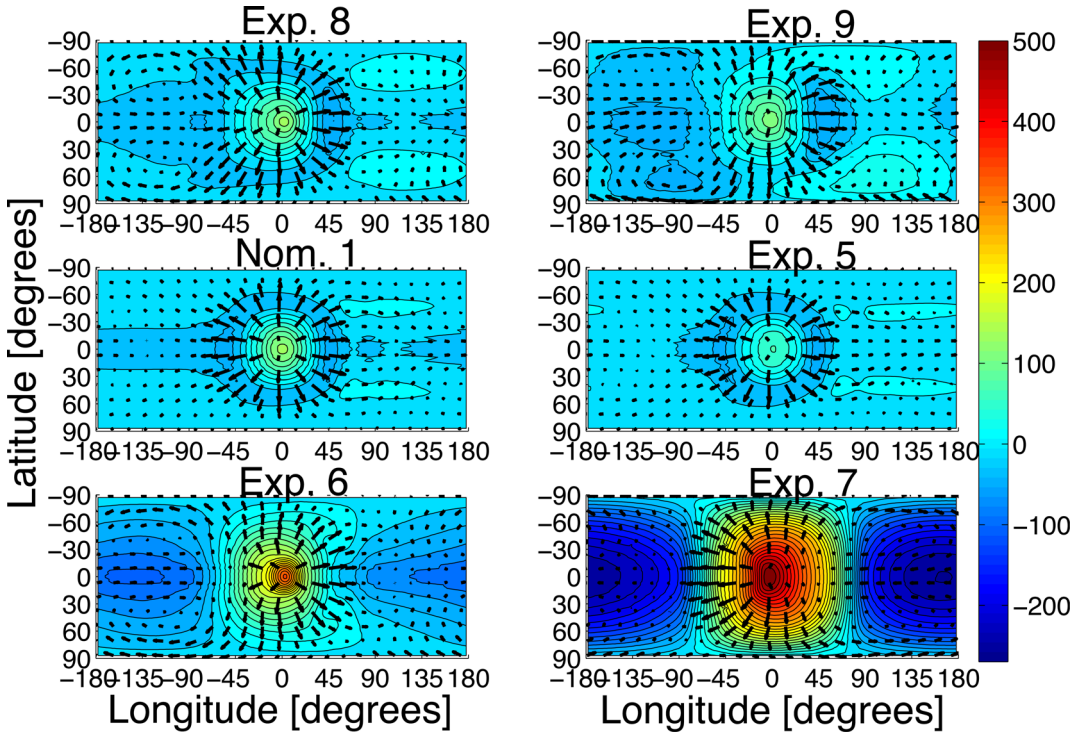

Figure 13. Eddy geopotential height in m and eddy horizontal wind in m s^{-1} at $p = 225$ mbar for the $P_{\rm rot} = 100$ d simulation of Exp.8 and Exp.9, the nominal model and Exp.5, Exp.6 and Exp.7. Contour levels are 20 m and the longest eddy wind vectors are left to right and from top to bottom 25.0, 34.4, 39.4, 37.8, 45.0 and 47.0 m s^{-1}, respectively.

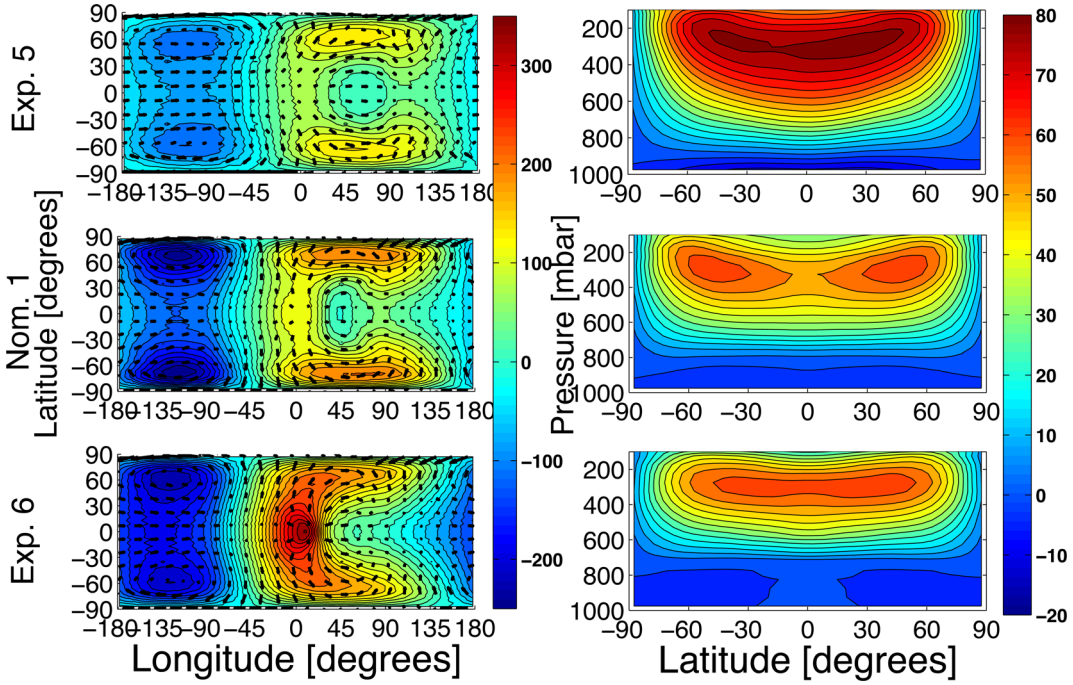

Figure 14. Left: eddy geopotential height in m and eddy horizontal wind in m s^{-1} at $p = 225$ mbar. Right: zonal mean of zonal wind in m s^{-1}. Both properties for the $P_{\rm rot} = 15$ d simulation of Exp.5, Nom.1 and Exp.6 from top to bottom. Contour levels of eddy geopotential heights are 20 m and the longest eddy wind vectors are from top to bottom 30.7, 47.0 and 44.3 m s^{-1}, respectively.

previous statement that Rossby wave gyres can form for $\lambda_{\rm R}/R_{\rm P}$ not much larger than unity. In Section 3.4.2, we associated the particularly strong thermal forcing, resulting from an increase in nightside cooling efficiency, with a stronger preference of tropical Rossby waves. Exp.8 and Exp.9 show deep negative geopotential perturbations over the nightside that are deeper than similar features in Exp.4. These perturbations indicate particularly cold nightside surfaces and thus stronger thermal forcing compared to the nominal model (Nom.2) but also to Exp.4. The triggered Rossby wave is therefore stronger in the slow rotation regime of Exp.8 and Exp.9 compared to Exp.4. The horizontal flow patterns at $p = 225$ mbar show equatorial jets instead of divergent flow over the substellar point for Exp.9 (Fig. 12). The abnormal climate state with easterly flow in Exp.7 may be triggered by even stronger thermal forcing due to a particularly cold nightside compared to Exp.8 and Exp.9.

Thus, we conclude that cold nightsides can trigger very strong thermal forcing between the dayside and the nightside that leads to climate states with either strong westerly or easterly flow. This flow can overcome the normal divergent flow on the top of the atmosphere for slow planet rotation ($P_{\rm rot} = 100$ d) and $\lambda_{\rm R}/R_{\rm P} = 1.75$.

4.2.3 Intermediate rotations with $\lambda_{\rm R}/R_{\rm P} \leq 1$

In Paper II, we found that the intermediate rotation region ($P_{\rm rot} <$ 34 d) is associated with the formation of efficient standing tropical Rossby waves. The coupling between Kelvin and Rossby waves becomes stronger with faster rotation, which leads to an acceleration of zonal winds. There is indeed a rise in zonal wind speeds with faster rotation between $P_{\rm rot} = 10$ and 35 d for all models except Exp.7 (Fig. 9). This indicates that the Rossby wave increases in strength with faster rotation periods also for Exp.8 and Exp.9, which were shown in the previous section to already have strong Rossby waves for relatively slow planet rotations.

The model with very efficient surface friction $t_{\rm s,fric} = 0.1$ d (Exp.5) experiences the strongest zonal wind acceleration with faster rotation in the intermediate rotation regime. Full acceleration is established at rotation period $P_{\rm rot} = 15$ d and continues with faster rotation until a new rotation regime is entered with $L_{\rm R}/R_{\rm P} \leq 1$ at $P_{\rm rot} = 10$ d (Fig. 9, upper panel). Apparently, the coupling between the standing Rossby waves and the Kelvin wave is more efficient with stronger surface friction in the intermediate rotation regime. This strong coupling can also be inferred from the eddy geopotential height field at $P_{\rm rot} = 15$ d (Fig. 14, top-left), which shows in contrast to Exp.1 and Nom.1 (Fig. 14, middle-left and bottom-left), a very weak ($z' \approx 75$ m) positive geopotential height anomaly over the substellar point, indicative of only weak upwelling from direct circulation. The fast equatorial superrotation that follows from the efficient Kelvin–tropical Rossby wave is also discernible as a broad strong equatorial westerly jet in the zonal mean of zonal winds of Exp.5 (Fig. 14, top-right).

The model with least efficient surface friction (Exp.7) exhibits an easterly jet even in the intermediate rotation regime, that is, for $P_{\rm rot} = 100$–12 d. For faster rotations than $P_{\rm rot} = 12$ d, the climate state changes abruptly. The eddy geopotential height and wind fields show between $P_{\rm rot} = 10$ and 14 d the beginning formation of tropical Rossby wave gyres over negative geopotential height perturbations at $\nu = \pm 30^\circ$ and $\phi = -160^\circ$ that are particularly evident for $P_{\rm rot} =$ 10 d (Fig. 15, left panels). The full formation of standing tropical Rossby waves is accompanied by a switch in the direction of zonal winds from easterly to westerly (Fig. 15, right panels, and Fig. 10 for $P_{\rm rot} = 10$–14 d). The standing tropical Rossby waves force Exp.7 into a normal superrotating state with faster and faster rotation.

The change in climate dynamics from an easterly towards a westerly flow in Exp.7 results in drastic changes in the temperatures and horizontal flow patterns at $p = 225$ mbar (Fig. 16). With the establishment of a climate state dominated by tropical Rossby waves and equatorial superrotation with $P_{\rm rot} \leq 10$ d, the cyclones flip from

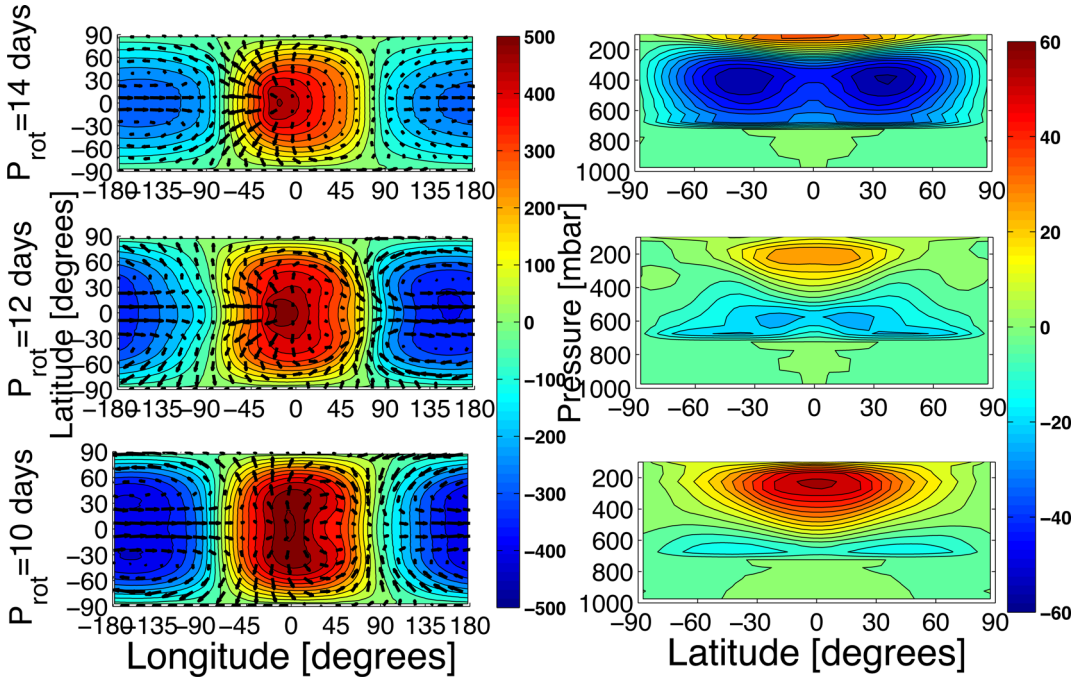

Figure 15. Left: eddy geopotential height in m and eddy horizontal wind in m s^{-1} at $p = 225$ mbar. Right: zonal mean of zonal wind in m s^{-1}. Both properties for Exp.7 and for rotation periods $P_{\rm rot} = 14$, 12 and 10 d from top to bottom. Contour levels of eddy geopotential heights are 50 m and the longest eddy wind vectors are from top to bottom 59.2, 44.7 and 47.5 m s^{-1}, respectively.

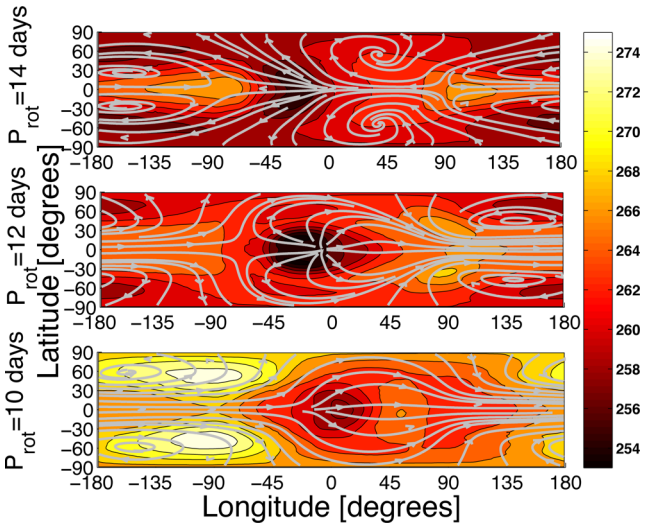

Figure 16. Temperatures (contour interval 2 K) and streamlines of the horizontal flow at $p = 225$ mbar for Exp.7 and for rotation periods $P_{\rm rot} = 14$, 12 and 10 d from top to bottom.

$\phi = +135^\circ$ to $\phi = -135^\circ$ and are then associated with local temperature maxima near the west terminator at $\phi = -35^\circ$ that are hotter than the temperatures found at $p = 225$ mbar for slower rotations (compare the middle and bottom panels of Fig. 16). Thus, the climate state with predominantly easterly flow has a smaller horizontal temperature gradient than the climate state with westerly flow and deep vortices.

Models with reduced PBL extent (Exp.8 and Exp.9) result in comparatively strong standing tropical Rossby wave gyres (not shown) and thus stronger equatorial superrotation, as evidenced by the larger zonal wind speeds compared to the nominal model (Fig. 9, bottom panel, between $P_{\rm rot} = 10$ and 35 d). In this respect, the models with reduced surface interface region are similar to Exp.4, which also showed better coupling between Kelvin and Rossby waves and thus likewise faster zonal wind speeds than the nominal model. This result confirms the conclusion drawn in the previous section that Exp.8 and Exp.9 represent models with particularly strong thermal forcing, which induce stronger tropical Rossby waves compared to the nominal model.

However, Exp.8 and Exp.9 never reach the level of strong coupling between Rossby and Kelvin waves as Exp.5 with the most efficient surface friction. We attribute the stronger zonal winds in Exp.8, Exp.9 and Exp.4 to the colder nightsides and thus larger dayside to nightside temperature gradients compared to the nominal model (Nom.1). Exp.7 shows that the nightside should not become too cold, otherwise the climate state may flip into a state with easterly instead of westerly winds. So, we conclude that there are two mechanisms to induce stronger equatorial superrotation: either a larger dayside to nightside temperature gradient or very efficient surface friction that triggers a stronger coupling between Kelvin and Rossby waves and thus faster equatorial superrotation. The latter appears to be effective only in the intermediate rotation regime.

4.2.4 Climate state bifurcation I: $L_{\rm R}/R_{\rm P} \leq 1$ and $\lambda_{\rm R}/R_{\rm P} \leq 0.5$

The climate simulations investigated in this section could, in principle, transit into a new rotation regime for $P_{\rm rot} \leq 10$ d. Because the extratropical Rossby wave becomes smaller than the planet size $L_{\rm R}/R_{\rm P} \leq 1$ (see Table 7), the extratropical Rossby wave can now also form a standing wave. This possible transition almost coincides with the tropical Rossby wave transition with $\lambda_{\rm R}/R_{\rm P} \leq 0.5$ at $P_{\rm rot} = 8$ d. We concluded in Paper II that the climate can thus enter two states in this rotation regime: one dominated by standing

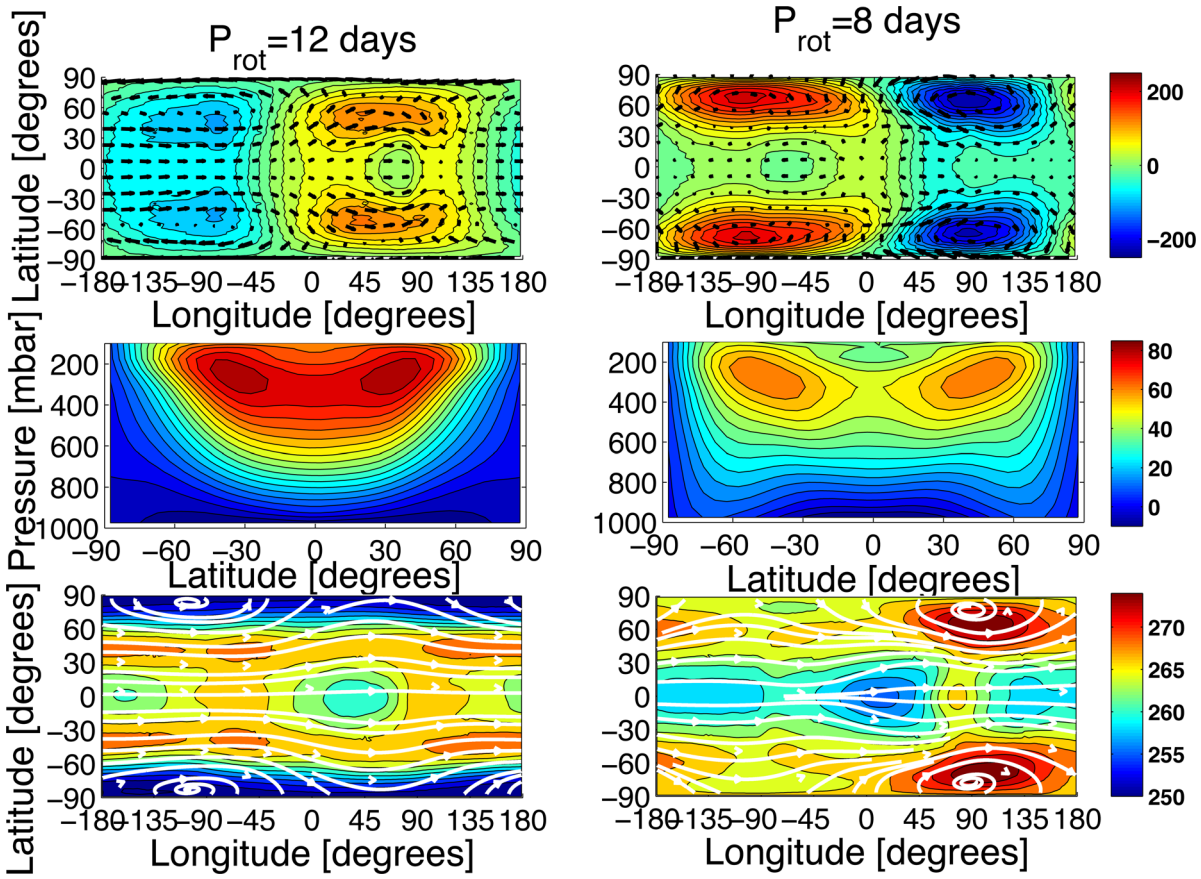

Figure 17. Top: eddy geopotential heights in m (contour interval 20 m) and eddy velocities (m s^{-1}). Middle: zonal mean of zonal winds in m s^{-1} (contour interval 5 m s^{-1}). Bottom: temperatures (contour interval 2 K) and streamlines of the horizontal flow at $p = 225$ mbar. The $P_{\rm rot} = 12$ d (left) and $P_{\rm rot} = 8$ d (right) simulations of Exp.5 are shown.

extratropical waves and high-latitude jets and one dominated by standing tropical Rossby waves and an equatorial jet, which gains in speed with faster rotation as soon as $\lambda_{\rm R}/R_{\rm P} < 0.5$. The formation of a standing extratropical Rossby wave can be inferred by an abrupt drop in zonal wind at the $L_{\rm R}/R_{\rm P} \leq 1$ transition with faster rotation, as shown by Edson et al. (2011) and discussed in Paper II. Models that remain in a climate state dominated by the tropical Rossby wave experience instead a smooth acceleration of zonal wind speeds with faster rotation around the $\lambda_{\rm R}/R_{\rm P} \leq 0.5$ transition, as demonstrated in Paper II.

The abrupt transition to lower zonal wind speeds near $L_{\rm R}/R_{\rm P} \leq 1$ can be seen for Exp.5 with $t_{\rm s,\,fric} = 0.1$ d (Fig. 9 between $P_{\rm rot} = 10$ and 12 d). The drop in zonal wind speeds is accompanied as expected by the formation of two high-latitude jets (Fig. 17, middle-right panel). The eddy geopotential height field shows at the same time the switch from a climate state dominated by tropical to a state dominated by extratropical Rossby wave gyres (compare Fig. 17, top panel, with fig. 2 of Paper II). The extratropical Rossby wave gyres are located at higher latitudes at $\nu = \pm 70^\circ$ compared to $\nu = \pm 45^\circ$ in the tropical Rossby wave state (Fig. 17, top panels). Also, the positive and negative geopotential height anomalies are shifted in longitude by about 180° with respect to each other. The negative geopotential height perturbations are located at $\phi = +90^\circ$ in the extratropical Rossby state and not at $\phi = -110^\circ$ as in the tropical Rossby state. The cyclones that are associated with the negative geopotentials also change location accordingly (Fig. 17, bottom panels).

The cyclones become again locations of warm temperature maxima after the switch to a climate state dominated by extratropical Rossby waves. We attribute the formation of temperature maxima to two effects: (i) upwelling is not suppressed by equatorial superrotation; (ii) the horizontal flow over the substellar point is not confined to the equator and can thus flow into the cyclones to become adiabatically heated (Paper II).

In Paper II, we already speculated that efficient surface friction may promote extratropical Rossby waves. Exp.5, the model with the most efficient surface friction, confirms this hypothesis and shows a climate state dominated by extratropical waves as soon as $L_{\rm R}/R_{\rm P} \leq 1$ with faster planet rotation. All other models remain in climate states dominated by tropical Rossby waves in this rotation regime with predominantly equatorial superrotation with relatively fast zonal wind speeds – at least as long as $L_{\rm R}/R_{\rm P} > 0.5$.

4.2.5 *Climate state bifurcation II: $L_{\rm R}/R_{\rm P} \leq 0.5$*

For even faster rotations ($P_{\rm rot} \leq 5$ d), another possible climate state transition is possible. We found in Paper II that these fast planet rotations allow for three different climate states: one with predominantly equatorial superrotation, one with two high-latitude westerly jets and one mixed climate state with features of both previously listed climate states. The latter is possible as both the tropical and extratropical Rossby waves can simultaneously fit on the planet in this planet rotation period regime; the Rossby radii of

deformation of both waves are smaller than half the planet's size. In Paper II, we found mixed states only for the smallest planet sizes ($R_P \leq 1.25\,R_{Earth}$).

In contrast to the results in Paper II, Exp.5 with $R_P = 1.45\,R_{Earth}$ assumes a climate state with high-latitude jets for fast planet rotations between $P_{rot} = 10$ and 2 d. Exp.5 evolves into a mixed climate state for $P_{rot} = 1.5$ d with the emergence of an additional equatorial jet (not shown). The existence of climate states with high latitude instead of strong equatorial superrotation can also be inferred from the zonal wind speed evolution of Exp.5 for $P_{rot} = 1.5$–2 d (Fig. 9, upper panel). Here, Exp.5 has lower wind speeds compared to other experiments.

Thus, we conclude that Exp.5 is qualitatively the most similar of our models to that of Edson et al. (2011). Exp.5 assumes the same climate states not only in the very short rotation period regime ($P_{rot} \leq 5$ d) but also in the short rotation period regime ($P_{rot} \leq 10$ d; see previous section). The wind speeds of Exp.5 are still 50 per cent larger than those reported by Edson et al. (2011).Exp.6 and Exp.7 with weak surface friction never form standing extratropical Rossby waves. Efficient surface friction favours the formation of standing extratropical Rossby wave.

The models with reduced PBL extent, Exp.8 and Exp.9, also assume mixed states between $P_{rot} = 2$ and 3 d. These climate states can again be inferred from the relatively low zonal wind speeds, in particular for Exp.9 (Fig. 9, lower panel). A compression in PBL extent, otherwise keeping $\tau_{s,\,fric} = 1$ d, is equivalent to raising surface friction efficiency in the very fast rotation period regime.

4.2.6 *Circulation*

Circulation is affected by every aspect of surface boundary variations. Here, we monitor the maxima and minima of the meridional mass stream function Ψ (see equation 8) on the Northern hemisphere, as introduced in Section 3.4.6, and we interpret the results for the expected circulation states: states 0–3 (see fig. 17 of Paper II). Generally, models with more efficient surface friction show stronger direct circulation (state 0) in the slow rotation regime ($P_{rot} \geq 35$ d), where one large circulation cell fills each hemisphere. Thus, Exp.5 has the greatest circulation strength Ψ_{max} in the slow rotation regime (Fig. 18). Direct circulation in Exp.7 is not only greatly diminished in strength compared to the other experiments, it also has particularly weak circulation efficiency near the surface, as close inspection of Ψ for $P_{rot} = 100$ d shows (Fig. 19).

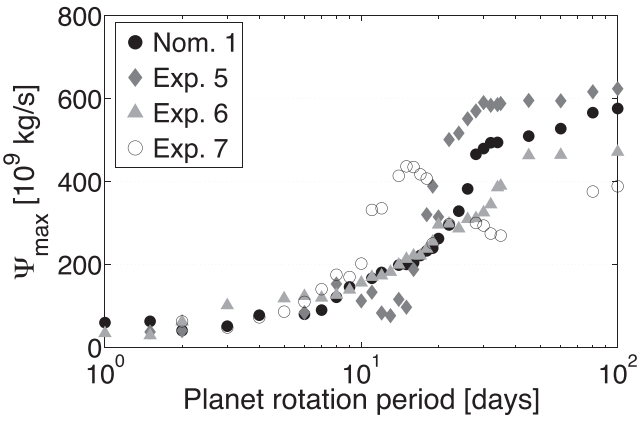

Figure 18. Maxima of the meridional mass transport stream function Ψ on the Northern hemisphere for the direct circulation cell for different surface friction time-scales and $R_P = 1.45\,R_{Earth}$ versus rotation period.

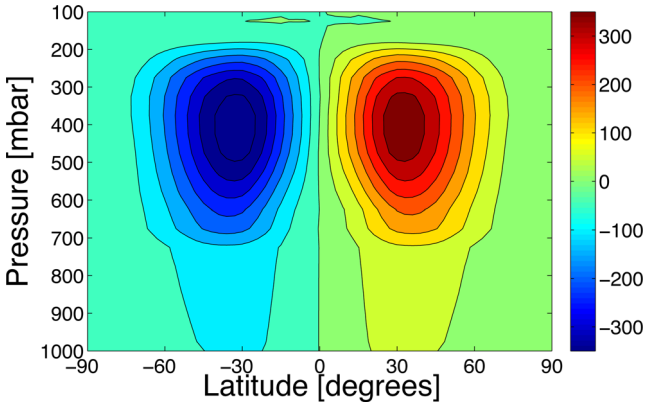

Figure 19. Meridional mass stream function Ψ in units of 10^9 kg s^{-1} for the $P_{rot} = 100$ d of Exp.7 with $t_{s,fric} = 100$ d, where positive values denote circulation in clockwise direction and negative values in counter-clockwise direction.

Table 8. Circulation cells.

	P_{rot} (d)			
	State 0	State 1	State 2	State 3
Exp.5	100–22	20–14	13–1.5	–
Nom.1	100–26	24–14	13–3	2–1
Exp.6	100–26	24–3	2–1[a]	–
Exp.7	100–11	10–2	–	–
Exp.8	100–45	35–18	17–2	1.5–1
Exp.9	100	80–20	22–2	1.5–1

Note. [a]Vertical break-up of circulation cells.

For faster planet rotation, more precisely for $P_{rot} \leq 34$ d, the formation of a new circulation state state 1 is expected, which we associated in Paper II with the formation of standing tropical Rossby waves that should form for $\lambda_R/R_P \leq 1$. Circulation state 1 does develop for the expected rotation periods for Nom.1, Exp.5 and Exp.6. State 1 is characterized by an embedded reverse circulation cell inside one large direct circulation cell per hemisphere, when monitoring the meridional mass stream function Ψ for latitude and pressure height (not shown, but see Table 8 for transition in circulation states based on the form and number of circulation cells in Ψ). The beginning formation of a state 1 circulation can also be inferred by the steep drop in Ψ_{max} with faster planet rotation for $P_{rot} \leq 34$ d in Nom.1, Exp.5 and Exp.6. However, the full formation of the embedded cells is discernible in the meridional stream function Ψ for faster rotations than $P_{rot} \approx 34$ d, which explains why full establishment of state 1 is apparent for $P_{rot} \approx 24$ d instead of $P_{rot} \approx 34$ d in Nom.1, Exp.5 and Exp.6 (Table 8). The deviation between Table 8 and the inferred onset of state 1 circulation from Ψ_{max} shows that the combined monitoring of the maximum strength of circulation cells (Ψ_{max}) and Rossby wavenumber transitions is necessary to fully interpret changes in the circulation cells in Ψ versus latitude and pressure height. The formation of new weak embedded circulation cells may not readily be apparent in the latter.[6]

In contrast to the models with nominal, strong and weak surface friction (Nom.1, Exp.5 and Exp.6), the circulation in the model with very inefficient surface friction (Exp.7) appears to gain strength for $P_{rot} \leq 34$ d. Ψ_{max} decreases again with faster rotation for $P_{rot} \leq 14$ d (Fig. 18). While we cannot explain the anomalous increase

[6] See Paper I for a more detailed discussion of state 1.

in circulation strength with faster planet rotation in Exp.7, we can explain the drop in circulation strength for $P_{\rm rot} \leq 14$ d. The latter is associated with the formation of state 1 circulation (Table 8). It coincides with the switch from a climate state with predominantly easterly winds and suppression of tropical Rossby waves ($P_{\rm rot} > 14$ d) to a climate state with fully formed standing tropical Rossby waves and westerly equatorial superrotation ($P_{\rm rot} \leq 10$ d). The switch was found in Section 4.2.3 between $P_{\rm rot} = 10$ and 14 d.

Embedded reverse cells are absent in Exp.7 for intermediate rotation periods ($P_{\rm rot} = 10$–34 d), because tropical Rossby waves are suppressed by the abnormal easterly flow. However, they appear as soon as the tropical Rossby waves fully form. Thus, circulation evolution with rotation period in Exp.7, Nom.1, Exp.5 and Exp.6 confirms that state 1 circulation is intricately linked to the presence of standing tropical Rossby waves (Paper II).

Exp.5 shows in the intermediate rotation regime $P_{\rm rot} = 10$–15 d a particularly strong embedded reverse circulation state 1. In Section 4.2.3, we have identified very efficient coupling between tropical Rossby and Kelvin waves for Exp.5 in this rotation regime. Apparently, this strong coupling also leads to stronger state 1 circulation. As a result, $\Psi_{\rm max}$ is particularly low for Exp.5 and $P_{\rm rot} = 10$–15 d (Fig. 18).

For even faster planet rotations ($P_{\rm rot} \leq 10$ d), Nom.1, Exp.6 and Exp.7 also show suppression of direct circulation as tropical Rossby waves, and thus equatorial superrotation strengthens. In contrast to Nom.1, Exp.6 and Exp.7, Exp.5 develops from a state with strong equatorial superrotation into a climate state dominated by extratropical Rossby waves for $P_{\rm rot} \leq 10$ d, as shown in Sections 4.2.4 and 4.2.5. The latter climate state prevents the formation of strong equatorial superrotation and thus maintains direct circulation. Indeed, for $P_{\rm rot} \approx 10$ d, the circulation strength $\Psi_{\rm max}$ increases for Exp.5 because equatorial superrotation disappears with faster rotation with the switch in climate state (Fig. 18). Because direct circulation strength generally decreases with faster rotation, $\Psi_{\rm max}$ does not reach the values for $P_{\rm rot} \geq 30$ d and decreases further in strength with faster rotation.

For $P_{\rm rot} = 10$–100 d, the simulations with compressed PBL (i.e. Exp.8 and Exp.9) show weaker direct circulation compared to the nominal model. The circulation strength is weaker the lower $p_{\rm PBL}$ is (Fig. 20, top panel). Furthermore, the experiments exhibit the appearance of embedded reverse cells (circulation state 1) for surprisingly slow planet rotations compared to other models (i.e. between $P_{\rm rot} = 40$ and 80 d; see Table 8). The onset of embedded circulation can be determined by the steep decline of the strength of the direct circulation cell (Fig. 20, top panel). In Section 3.4.6, we have associated embedded reverse cells with standing tropical Rossby waves. These form in the nominal model in a rotation period regime for which $\lambda_{\rm R}/R_{\rm P} \leq 1$. However, Exp.8 and Exp.9 have already been shown to form tropical Rossby waves at $P_{\rm rot} = 100$ d for $\lambda_{\rm R}/R_{\rm P} = 1.75$ (Section 4.2.2). We concluded then that tropical Rossby waves can form under special circumstances – as presented by Exp.8. and *9* – for $\lambda_{\rm R}/R_{\rm P}$ larger than unity. The Rossby waves in the slow rotation regime are apparently strong enough to induce state 1 circulation for comparatively slow planet rotators compared to Nom.1. This result confirms that embedded reverse cells are inherent properties of climate states with standing tropical Rossby waves, at least in our model prescription.

Models with reduced PBL extent not only develop circulation state 1 for slow planet rotation, they also develop circulation states with more than one fully vertically extended circulation cell per hemisphere (i.e. circulation state 2 for slower planet rotations compared to the nominal model, Nom.1). The formation of circulation

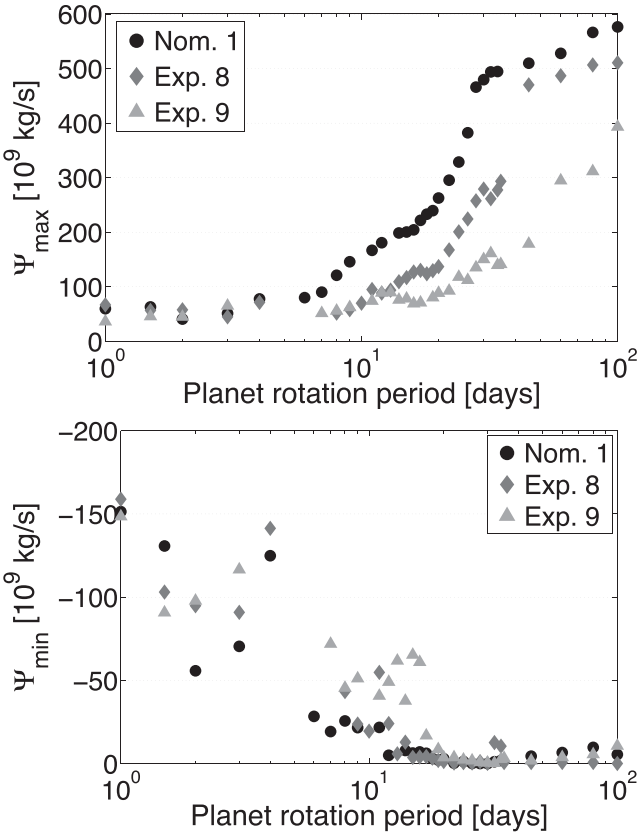

Figure 20. Maxima of the meridional mass transport stream function Ψ on the Northern hemisphere for the direct circulation cell (top) and minima of the secondary circulation cell (bottom) for various PBL extents and $R_{\rm P} = 1.45\,R_{\rm Earth}$ versus rotation period.

state 2 can be inferred from Table 8 and Fig. 20 (lower panel). The latter shows the substantial strengthening of the secondary circulation cells for $P_{\rm rot} \approx 22$–17 d. Thus, although direct circulation is suppressed by the tropical Rossby waves, the role of circulation can be taken over by the secondary circulation cells that are not affected by equatorial superrotation. In addition, we note that the strength of the secondary circulation cell is greater for models with compressed PBL (Exp.8 and Exp.9) compared to the nominal model (Nom.1).

There are two climate state bifurcations in the short rotation period regime (i.e. for $P_{\rm rot} \leq 10$ d). One bifurcation exists around $P_{\rm rot} \approx 10$ d and can lead to climate state transitions for the extratropical ($L_{\rm R}/R_{\rm P} < 1$) or tropical Rossby wave ($\lambda_{\rm R}/R_{\rm P} < 0.5$). The other bifurcation point exists at the extratropical Rossby wavenumber $L_{\rm R}/R_{\rm P} \approx 0.5$ (i.e. at $P_{\rm rot} \approx 5$ d). Consequently, there are several possible climate states with different circulation patterns for $P_{\rm rot} \leq 10$ d, as evidenced by the strong fluctuation in strength of the secondary circulation cells (Fig. 20, lower panel).

In general, climate states dominated by tropical Rossby waves and thus equatorial superrotation show a vertically compressed direct circulation cell that is often vertically fragmented by embedded reverse circulation (see fig. 17 in Paper II). Circulation state 2 can lead to a stabilization of circulation cells. Climate states dominated by standing extratropical Rossby waves have unperturbed direct circulation cells at the equator. Exp.5 is in this state in the short rotation regime ($P_{\rm rot} \leq 3$ d). It is shown in the following section that the changes in circulation states due to different climate states also result in different surface temperature evolutions.

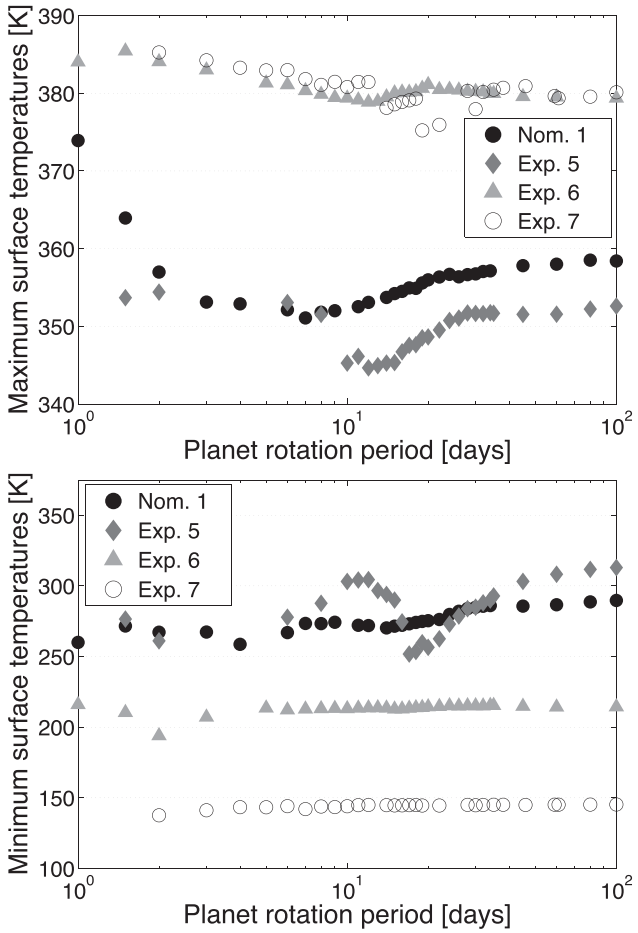

Figure 21. Maximum and minimum surface temperatures for different surface friction time-scales $t_{s,fric} = 0.1$–100 d and $R_P = 1.45\,R_{Earth}$.

4.2.7 Surface temperatures and habitability

The surface temperatures in the models with the least efficient surface friction (Exp.6 and Exp.7 with $t_{s,fric} = 10$ and 100 d, respectively) are basically decoupled from atmosphere dynamics. They do not evolve with changes in climate states and circulation structure in the whole rotation period regime (Fig. 21). However, the surface temperatures exhibit huge differences between the dayside and nightside with $\Delta T = 110$ and 230 K for Exp.6 and Exp.7, respectively. In particular, the nightside is adversely affected by the reduction in heat transfer near the surface and assumes very cold surface temperatures of $T_{NS,s} = 220$ and 150 K, respectively. At no point, however, do the models reach temperatures that would lead to out-freezing of the primary atmosphere component. The dayside surface temperatures are comparatively less affected by the inefficiency of heat transport and, at the substellar point, reach temperatures of $T_{DS,s} \approx 380$ K. These substellar point temperatures can also be reached for fast rotating tidally locked planets ($P_{rot} = 1$ d) if strong equatorial superrotation suppresses cooling of the substellar point via upwelling (Nom.1). The very cold nightsides were already inferred in Section 4.2.2 from the very deep negative geopotential height perturbation. Thus, we confirm here that Exp.6 and Exp.7 have a particularly large dayside to nightside temperature gradient ΔT.

Although the surface temperatures are apparently unaffected by different climate states for experiments with weak surface friction, the very cold nightside temperatures and the large temperature gradient, in turn, influence climate states, in particular for slow and intermediate rotations ($P_{rot} = 12$–100 d). The resulting strong negative geopotential anomalies z' lead to stronger Kelvin and Rossby waves for $P_{rot} = 100$ d. For $z' \leq 200$ m or $T = 150$ K at the nightside in Exp.7, we even find a change in zonal wind direction from an equatorial westerly (superrotation) to equatorial easterly flow (antirotation).

The surface temperatures of experiments with efficient surface friction $t_{s,fric} \leq 1$ d (Exp.5 and Nom.1) evolve with planet rotation. Generally, the nightside and surface temperatures cool down with faster rotation between $P_{rot} = 100$ and 10 d. However, Exp.5 deviates between $P_{rot} = 10$ and 15 d from this nominal evolution outlined in Paper II. As shown previously (Section 4.2.3), in this rotation regime Exp.5 experiences a climate state with particularly strong coupling between standing tropical Rossby and Kelvin waves. This strong coupling leads to a weakening of the direct circulation (see previous section, Fig. 18). At the same time, secondary circulation cells are weak in the relevant rotation regime (Table 8). Thus, we would expect warmer substellar point temperatures and colder nightside temperatures compared to slower planetary rotation. Surprisingly, the exact opposite is observed (Fig. 21). Either the relative strength of the embedded reverse circulation (state 1) provides an alternative heat transport mechanism between $P_{rot} = 10$ and 15 d in Exp.5 or the overall weakness in the vertically fragmented direct equatorial cells is compensated by more efficient heat transport close to the surface in the lower branch of the direct circulation cell.

The evolution of the dayside surface temperatures in the experiments with compressed PBL (Exp.8 and Exp.9) shows generally the same evolution with rotation period as the nominal model (Nom.1). The surface temperatures are just warmer by a few Kelvin if the PBL extent is compressed (Fig. 22, upper panel).

The evolution of the nightside surface temperatures is more strongly affected by changes in climate states. The nightside surface temperatures show variations of up to 32 K for changes in the PBL extent (Fig. 22, lower panel). For slow rotators ($P_{rot} =$ 40–100 d), less heat reaches the nightside via direct circulation the more compressed the PBL is.

In the intermediate to slow rotation regime ($P_{rot} =$ 10–40 d), Exp.8 and Exp.9 show a very different nightside temperature evolution with faster planet rotation compared to the nominal model (Nom.1): the nightside surface temperatures rise steeply with faster planet rotation. A new heat transport mechanism develops in this rotation regime, which becomes more and more efficient with faster rotation.

One obvious candidate for such a heat transport mechanism is secondary circulation cells (circulation state 2) that start to develop for surprisingly slow rotations for experiments with compressed PBL and gain in strength with faster rotation (Fig. 20, lower panel, and Table 8). Closer comparison between the increase in nightside surface temperatures with faster rotation and the development of circulation state 2 shows that both do not match in rotation period phase space. Circulation state 2 forms for $P_{rot} \leq$ 17–22 d and the nightside surface temperatures increase for $P_{rot} \leq 30$ and 40 d in Exp.8 and Exp.9, respectively (compare Table 8, Fig. 20, lower panel, and Fig. 22, lower panel).

Because direct circulation strength decreases with faster rotation in Exp.8 and Exp.9, we conclude that there is only one mechanism that can explain the warming of the nightside with faster rotation in the intermediate to slow rotation regime ($P_{rot} =$ 10–40 d): the embedded reverse circulation cells of circulation state 1. These are already present for $P_{rot} = 30$ and 40 d, respectively (see previous

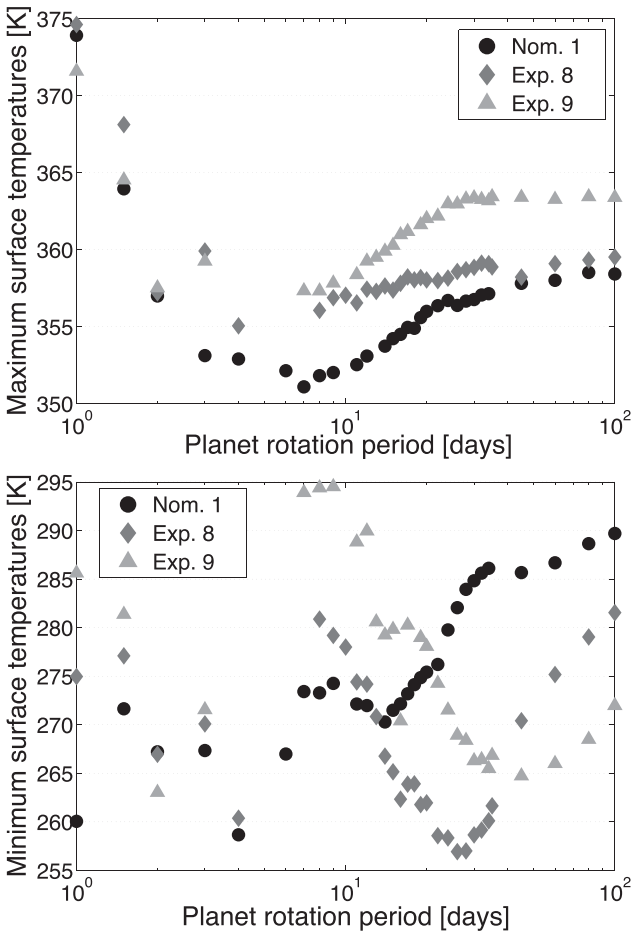

Figure 22. Maximum and minimum surface temperatures for different PBL extent $p_{\rm PBL} = 700$–900 mbar and $R_{\rm P} = 1.45\,R_{\rm Earth}$.

section) and it was shown in Paper II that they also gain in strength with faster planet rotation.

We speculate that the nightside surface is not warmed in the nominal model (Nom.1) by embedded reverse cells, because the cells are located above the PBL. $p_{\rm PBL} = 700$ mbar is relatively high in Nom.1 (see Paper I). If the upper extent of the PBL is lowered, so is the location of the embedded reverse cell. The closer the embedded reverse cell comes to the surface, the more heat it can transport towards the surface's nightside.

For fast planet rotation ($P_{\rm rot} \leq 10$ d), the embedded circulation cells do not transport heat any longer and the nightside surface temperatures of Exp.8 and Exp.9 again follow qualitatively the evolution of Nom.1 with faster planet rotation.

5 SUMMARY

We have investigated how variations in nightside cooling efficiency, surface friction time-scales and PBL height affect the climate states of tidally locked Earth-like planets. This is the first study that covers, for every scenario, the rotation period between $P_{\rm rot} = 1$ and 100 d to also take into account changes in climate states as identified in Paper II.

We performed a series of nine parametric scans, where we took advantage of the versatility of our model. First, we varied the thermal forcing, as follows.

(i) In Exp.1, the thermal forcing on the nightside of a Super-Earth planet ($R_{\rm P} = 1.45\,R_{\rm Earth}$) was increased by gradually reducing the radiative time-scale on the nightside from $t_{\rm rad,NS} = 813$ to $t_{\rm rad,NS} = 100$ d.

(ii) In Exp.2, the optical depth was increased from $\tau_{\rm s} = 0.62$ to $\tau_{\rm s} = 0.94$.

(iii) In Exp.3, the planet size was reduced from $R_{\rm P} = 1.45\,R_{\rm Earth}$ to $R_{\rm P} = 1\,R_{\rm Earth}$, using the same thermal forcing as for Exp.2.

(iv) In Exp.4, the radiative time-scales on dayside and nightside were decreased by a factor of 1.45 to compensate for increased efficiency of dynamics due to the decrease in planet size between Exp.2 and Exp.3.

We find that an increase in nightside cooling efficiency lowers the nightside surface temperatures significantly by about 80–100 K in Exp.1, while the dayside surface temperatures are lowered at the same time by 25 K at most.

In our model, an increase in optical depth – keeping all other parameters equal – affects mainly the dayside, as shown by Exp.2. The dayside surface temperatures $T_{\rm DS,s}$ rise and the radiative time-scale decreases with increasing optical depth, which leads to a combined overall hotter dayside despite more vigorous circulation. In contrast, a similar experiment conducted by Joshi et al. (1997) showed that an increase in optical depth in their model led to a rise in the nightside surface temperatures. Joshi et al. (1997) explicitly state that the radiative time-scales in their simplified thermal forcing prescription were unaffected by changes in optical depth. The effect of changes in optical depth can thus only be due to an increase in circulation.

Exp.3 demonstrated that a reduction in planet size – keeping all other parameters equal – leads to a reduction of the temperature gradient between the dayside and the nightside. In particular, the nightside is substantially warmer in Exp.3 compared to Exp.2. Exp.3 thus confirms the results reported by Joshi et al. (1997), that is, stronger circulation – keeping radiative time-scales equal – leads to a rise in nightside surface temperatures.

Exp.4 demonstrated that the dynamical time-scale is scaled to first order with $\sim R_{\rm P}$. Stronger circulation in Exp.3 compared to Exp.2 can thus successfully be compensated by lowering the radiative time-scales by a factor of 1.45 to account for reduction in planet size from $R_{\rm P} = 1.45\,R_{\rm Earth}$ to $R_{\rm P} = 1\,R_{\rm Earth}$. As a result, the dayside and nightside surface temperatures in Exp.2 and Exp.4 are similar to each other.

Exp.4 was found to assume for all intermediate to fast rotation periods $P_{\rm rot} = 1$–26 d a climate state dominated by standing tropical Rossby waves and equatorial superrotation. The nominal model for an Earth-sized planet and with inefficient nightside cooling (Nom.2) was reported in Paper II to also favour climate states with standing tropical Rossby waves in the intermediate rotation regime $P_{\rm rot} =$ 4–26 d. In the fast planet rotation regime, however, in contrast to Exp.4 Nom.1 showed the formation of standing extratropical Rossby waves with two high-latitude westerly jets instead of, or in addition to, an equatorial jet. The latter climate states are called mixed states.

Exp.4 has stronger thermal forcing than the nominal model for the same planet size with $R_{\rm P} = 1\,R_{\rm Earth}$ (Nom.2) because of larger optical depth and more efficient nightside cooling. We conclude that the stronger thermal forcing favours the formation of standing tropical Rossby waves. It suppresses the formation of standing extratropical Rossby waves for $P_{\rm rot} = 1.5$–3 d. Thus, we have identified strong thermal forcing as one mechanism that drives the model to favour

one possible climate state in the short rotation period regime over the other. Despite strong thermal forcing, the model used by Edson et al. (2011) does not suppress standing extratropical Rossby waves in the fast rotation regime. Thermal forcing can thus only be one possible component that determines which climate state a rocky tidally locked planet assumes in the short rotation period regime.

In the second part of our parameter study, we varied surface boundary treatments. We changed the following:

(i) surface friction time-scale to $t_{\rm s,fric} = 0.1$, 10 and 100 d (Exp.5, Exp.6 and Exp.7, respectively);
(ii) the upper extent of the planet boundary layer to $p_{\rm PBL} = 800$ and 900 mbar (Exp.8 and Exp.9, respectively);
(iii) $R_{\rm P} = 1.45\,R_{\rm Earth}$ and the nominal thermal forcing was assumed for surface boundary treatment variations.

We found large climate state differences in the whole rotation period regime ($P_{\rm rot} = 1$–100 d) for surface friction and boundary layer variations.

Most notably, Exp.5 assumes climate states dominated by the extratropical Rossby wave with two high-latitude westerly jets in the fast rotation regime ($P_{\rm rot} \leq 10$ d), in contrast to all other experiments. For very fast rotations ($P_{\rm rot} \leq 2$ d), Exp.5 exhibits mixed climate states with both tropical and extratropical standing Rossby waves. Therefore, we have identified the second mechanism that determines which climate state a rocky tidally locked planet assumes in the short rotation period regime in addition to strength of thermal forcing (i.e. surface friction efficiency). Apparently, strong surface friction favours the formation of standing extratropical Rossby waves as soon as the Rossby wavenumber $L_{\rm R}/R_{\rm P}$ becomes smaller than unity. Showman & Polvani (2011) speculated that surface friction might be one mechanism on rocky planets that may give rise to climate dynamics that deviate from tropical Rossby waves exhibited by gas planets.

Interestingly, for intermediate rotations ($P_{\rm rot} = 10$–15 d), where extratropical Rossby waves cannot form because $L_{\rm R}/R_{\rm P} > 1$, Exp.5 assumes a climate state with particularly strong coupling between standing tropical Rossby and Kelvin waves. This coupling leads not only to very strong equatorial winds but also to suppressed direct circulation and strong embedded reverse circulation.

Experiments with weaker surface friction efficiency than the nominal model (i.e. Exp.6 and Exp.7) show decoupling between the surface temperatures and circulation: the surface temperatures hardly change in the investigated rotation period regime ($P_{\rm rot} = 1$–100 d) and the nightside surface assumes very cold temperatures ($T_{\rm NS,s} = 220$ and 150 K for Exp.6 and Exp.7, respectively). While surface temperatures do not evolve with rotation period and are thus not affected by changes in climate states, the cold nightsides affect the possible climate states instead, in particular in the slow and intermediate rotation regime ($P_{\rm rot} = 12$–100 d).

In the intermediate to slow rotation regime ($P_{\rm rot} = 10$–100 d), simulations with very cold nightside surface temperatures, $T_{\rm NS,s} \leq 220$ K (i.e. Exp.6 and also Exp.4), trigger stronger tropical Rossby waves, which lead to stronger equatorial superrotation. Exp.7 with the coldest nightside ($T_{\rm NS,s} \approx 150$ K) shows, surprisingly, a drastically different climate state for intermediate to slow planet rotation: it exhibits strong easterly winds ($u = -50$ to $-80\,{\rm m\,s^{-1}}$). They even appear to suppress the formation of tropical Rossby waves with faster planet rotation. The strength of the easterly wind in Exp.7 diminishes with faster rotation and eventually the wind system displays normal westerly equatorial superrotation, albeit for comparatively fast rotations ($P_{\rm rot} \leq 12$ d). The onset of westerly superrotation is accompanied by the formation of standing tropical Rossby waves. We are currently at a loss to explain the peculiar behaviour of Exp.7 and tentatively link it to the extremely cold nightside exhibited in that experiment.

When the PBL is more compressed (Exp.8 and Exp.9), the simulations develop colder nightside surface temperatures than the nominal model in the slow rotation regime. However, they do not reach the temperatures of models with very weak surface friction (Exp.6 and Exp.7): they assume $T_{\rm NS,s} = 255$ and 265 K, respectively.

Surprisingly, Exp.8 and Exp.9 – and also Exp.4 with efficient nightside cooling – show tropical Rossby wave gyres in the slow rotation regime ($P_{\rm rot} = 100$ d). We conclude that for very strong thermal forcing in our model prescription, Rossby wave gyres can form for $\lambda_{\rm R}/R_{\rm P}$ larger than unity: $\lambda_{\rm R}/R_{\rm P} = 1.75$–2. Closer inspection of flow and geopotential perturbations for $\lambda_{\rm R}/R_{\rm P} \approx 1$ confirmed that full formation of tropical Rossby waves takes place solely in the $\lambda_{\rm R}/R_{\rm P} < 1$ regime (i.e. for $P_{\rm rot} < 34$ d). As a side note, although the dry model used by Edson et al. (2011) appears to have similar strength in thermal forcing as Exp.4, they do not report weak Rossby waves for $P_{\rm rot} = 100$ d. However, we have already concluded that thermal forcing alone does not determine which planetary wave can form. At least surface friction has to be taken into account as well. Unfortunately, we do not know how efficient surface friction is in Edson et al. (2011).

Another surprise was found for the experiments with compressed PBL (Exp.8 and Exp.9) in the intermediate to slow rotation regime $P_{\rm rot} = 10$–100 d. The tropical Rossby wave is capable of triggering the formation of embedded reverse cells for slow rotations. Furthermore, these cells appear to transport heat efficiently from the dayside towards the nightside between $P_{\rm rot} = 10$ and 40 d. The fact that we only find embedded reverse cells in climate states with tropical Rossby waves, and that these are completely suppressed otherwise (e.g. in Exp.7 for $P_{\rm rot} = 12$–100 d), confirms the conclusion in Paper II that these features are exclusively linked to tropical planetary waves.

6 CONCLUSION AND OUTLOOK

This study provides a coherent link between climate states and basic assumptions in thermal forcing and frictional solid surface boundaries. Because of the computational efficiency of our model, we could perform many experiments (ca. 700 experiments including Paper II) that cover the relevant rotation period $P_{\rm rot} = 1$–100 d in fine detail. Our study provides a better understanding of how surface temperatures and circulation can vary between different climate models for tidally locked terrestrial planets. This understanding is particularly important for rocky planets on relatively tight orbits, whose atmosphere properties will become first accessible to observations.

We found that strong surface friction ($t_{\rm s,fric} = 0.1$ d) promotes the formation of extratropical Rossby waves for fast rotating terrestrial planets ($P_{\rm rot} \leq 10$ d), as already noted by Showman & Polvani (2011). This rotation period region is of relevance for the extended inner habitable zone that ranges at least down to $P_{\rm rot} = 6$ d for M dwarf stars (Seager 2013; Zsom et al. 2013). It is also of relevance for the model of Yang et al. (2014) who found that the inner edge of the habitable zone can be expanded towards the star for tidally locked planets due to cloud coverage over the substellar point. Cloud formation over the substellar point is only possible with unperturbed upwelling over the substellar point and thus unperturbed direct circulation cell. The latter requires climate states that are dominated by standing extratropical Rossby waves in the fast rotation regime. Otherwise, equatorial superrotation brought about by the formation

of standing tropical Rossby waves would disrupt direct circulation. Thus, as discussed in Paper II, different circulation states in the short rotation regime yield different prospects on habitability.

Surface friction alone, however, is not the only mechanism that determines which planetary wave and thus climate state can form on a tidally locked rocky planet with fast rotation. Also, thermal forcing was found to play a strong role: stronger thermal forcing (e.g. due to very efficient nightside cooling) was found to lead to a climate state dominated by tropical standing Rossby waves rather than extratropical Rossby waves.

In addition, not only surface friction in terrestrial planets but also friction in gas planets can, apparently, excite climate states that are not exclusively dominated by equatorial superrotation. For the Hot Jupiter WASP-43b, Kataria et al. (2015) report an evolution from a climate state with an equatorial superrotating jet to a mixed state with two westerly high-latitude jets and an equatorial jet, if frictional drag is uniformly increased from $t_{\rm fric} = 10^6$ s to 10^5 s. Thus, our study can be linked to the study of Hot Jupiters.

Thus, we will develop our model further to encompass also the highly interesting hot Super-Earths in the intermediate region between terrestrial and gas planets. We will investigate if planets with a solid surface are indeed in a different climate state than planets without a solid boundary, and if climate state differences could be potentially observed by, for example, the upcoming *James Webb Space Telescope* (*JWST*).

Furthermore, we will address how ambiguities can be solved (e.g. how to disentangle surface drag from other drag mechanisms that may be present in gas planets). Surprisingly, Kataria et al. (2014) showed that even changes in atmosphere composition can induce a change in climate state. Atmospheres with high molecular mean weight such as CO_2 can likewise exhibit a mixed state with high-latitude jets and a weak equatorial jet. They only compared a few simulations. Thus, we plan to explore the hot Super-Earth climate regime with more experiments to resolve ambiguities and to investigate the reliability of model results in order to pave the way for the observations of smaller exoplanets.

ACKNOWLEDGEMENTS

We acknowledge support from the KU Leuven projects IDO/10/2013 and GOA/2015-014 (2014-2018 KU Leuven). The computational resources and services used in this work were provided by the Flemish Supercomputer Center (VSC), funded by the Hercules Foundation and the Flemish Government department EWI. Furthermore, we wish to thank the anonymous referee whose insightful remarks and suggestions led to a substantial improvement in the quality of this paper.

REFERENCES

Adcroft A., Campin J.-M., Hill C., Marshall J., 2004, Monthly Weather Review, 132, 2845
Carone L., Keppens R., Decin L., 2014, MNRAS, 445, 930 (Paper I)
Carone L., Keppens R., Decin L., 2015, MNRAS, 453, 2412 (Paper II)
Charbonneau D. et al., 2009, Nat, 462, 891
Correia A. C. M., Levrard B., Laskar J., 2008, A&A, 488, L63
Edson A., Lee S., Bannon P., Kasting J. F., Pollard D., 2011, Icarus, 212, 1
Gill A. E., 1980, Quarterly Journal of the Royal Meteorological Society, 106, 447
Held I. M., Suarez M. J., 1994, Bulletin of the American Meteorological Society, 75, 1825
Heng K., Vogt S. S., 2011, MNRAS, 415, 2145
Holton J. R., 1992, An Introduction to Dynamic Meteorology. Academic Press, San Diego
Joshi M., 2003, Astrobiology, 3, 415
Joshi M. M., Haberle R. M., Reynolds R. T., 1997, Icarus, 129, 450
Kaltenegger L., Traub W. A., 2009, ApJ, 698, 519
Kataria T., Showman A. P., Fortney J. J., Marley M. S., Freedman R. S., 2014, ApJ, 785, 92
Kataria T., Showman A. P., Fortney J. J., Stevenson K. B., Line M. R., Kreidberg L., Bean J. L., Désert J.-M., 2015, ApJ, 801, 86
Leconte J., Forget F., Charnay B., Wordsworth R., Selsis F., Millour E., Spiga A., 2013, A&A, 554, A69
Leconte J., Wu H., Menou K., Murray N., 2015, Sci, 347, 632
Madhusudhan N., Redfield S., 2015, International Journal of Astrobiology, 14, 177
Marshall J., Adcroft A., Campin J.-M., Hill C., White A., 2004, Monthly Weather Review, 132, 2882
Matsuno T., 1966, Journal of the Meteorological Society of Japan, Series II, 44, 25
Menou K., 2012, ApJ, 744, L16
Merlis T. M., Schneider T., 2010, Journal of Advances in Modelling Earth Systems, 2, 13
Molteni F., 2002, Climate Dynamics, 20, 175
Navarra A., Boccaletti G., 2002, Climate Dynamics, 19, 467
Polvani L. M., Kushner P. J., 2002, Geophys. Res. Lett., 29, 1114
Seager S., 2013, Sci, 340, 577
Showman A. P., Polvani L. M., 2011, ApJ, 738, 71
Showman A. P., Cho J. Y-K., Menou K., 2010, in Seager S., ed., Exoplanets. University of Arizona Press, Tucson, AZ, p. 471
Yang J., Cowan N. B., Abbot D. S., 2013, ApJ, 771, L45
Yang J., Boué G., Fabrycky D. C., Abbot D. S., 2014, ApJ, 787, L2
Zsom A., Seager S., de Wit J., Stamenković V., 2013, ApJ, 778, 109

This paper has been typeset from a TEX/LATEX file prepared by the author.